Eur. Phys. J. A **17**, 245–267 (2003)
DOI 10.1140/epja/i2002-10145-2

THE EUROPEAN PHYSICAL JOURNAL A

Experimental evidence for narrow baryons in the mass range $1.0 \leq M \leq 1.46$ GeV

B. Tatischeff[1,a], J. Yonnet[1], M. Boivin[2], M.P. Comets[1], P. Courtat[1], R. Gacougnolle[1], Y. Le Bornec[1], E. Loireleux[1], M. MacCormick[1], F. Reide[1], and N. Willis[1]

[1] Institut de Physique Nucléaire, CNRS/IN2P3, F–91406 Orsay Cedex, France
[2] Laboratoire National Saturne, CEA/DSM CNRS/IN2P3, F–91191 Gif-sur-Yvette Cedex, France

Received: 3 July 2002 / Revised version: 28 January 2003 /
Published online: 5 June 2003 –
Communicated by M. Garçon

Abstract. The reaction pp $\rightarrow$ pπ^+X was studied at different incident energies around $T_{\rm p} = 2$ GeV. Narrow baryonic structures were observed in the missing mass $M_{\rm X}$ and in the invariant mass $M_{\rm p\pi^+}$. The masses of these structures are 1004, 1044, 1094, 1136, 1173, 1249, 1277, and 1384 MeV (and possibly 1339 MeV). Some of them were also observed at the same masses in the missing-mass spectra of the dp $\rightarrow$ ppX reaction although with a weaker signature. Many checks were performed to make sure that these structures were not produced by experimental artifacts. Several narrow small-amplitude peaks, were also extracted using already published photonucleon cross-sections. The small widths of all these results, and the stability of the observed structures, regardless of the experiment, were used to conclude that they are genuine baryons and not merely the consequence of dynamical rescatterings. These baryons cannot be associated with classical q^3 quark configurations. We associate them with two colored-quark cluster configurations.

PACS. 14.20.Gk Baryon resonances with $S = 0$ – 12.40.Yx Hadron mass models and calculations – 13.75.Cs Nucleon-nucleon interactions (including antinucleons, deuterons, etc.) – 14.20.Pt Dibaryons

1 Introduction

For a number of years narrow structures have been observed in hadronic spectra. Isovectorial dibaryons were first observed [1] (and references therein), then other narrow dibaryon isospin states [2]. Narrow structures were also observed in baryons [3] and in mesons [4–6]. Since these structures were observed at stable masses, whatever the reaction, incident energy or production angle, they were associated with real hadrons and not with final-state rescatterings. There is no room for new low-mass mesons within the many-quark models for mesons that consider only $q\bar{q}$ configurations, given the excellent agreement between observation and calculation [7]. Once again there is no room in the mass range $M \leq 1.5$ GeV for new baryons within the many-quark models for baryons, if we consider only qqq configurations. The classical hadronic spectrum, which corresponds to broad resonances, is rather well understood. This is not the case for the narrow structures reported.

Preliminary results concerning the three first exotic baryons have previously been published [3]. The present paper

- gives a complete description of the experiment, the analysis and the checks performed,
- presents indications of new structures at higher masses, less clearly excited,
- compares our mass structures to narrow mass structures observed in other experiments,
- discusses the various attemps to relate these observations to physical explanations.

This paper is constructed in the following way: in sect. 2 we describe the detector performances and the data processing. In sect. 3 the various normalizations applied to obtain the cross-sections will be described. The simulation used in evaluating these normalizations and to test the complete experimental device will be discussed in sect. 4 whereas the various checks performed in order to underline our confidence in the genuine reality of the observed structures are presented in sect. 5. In sect. 6 the results of our two experiments are presented, namely:

- The pp $\rightarrow$ pπ^+X reaction, studied at three incident energies: $T_{\rm p} = 1.52$ GeV, 1.805 GeV, and 2.1 GeV and several forward angles. Narrow baryons were looked for in the missing mass $M_{\rm X}$ and in the invariant mass $M_{\rm p\pi^+}$.

[a] e-mail: tati@ipno.in2p3.fr

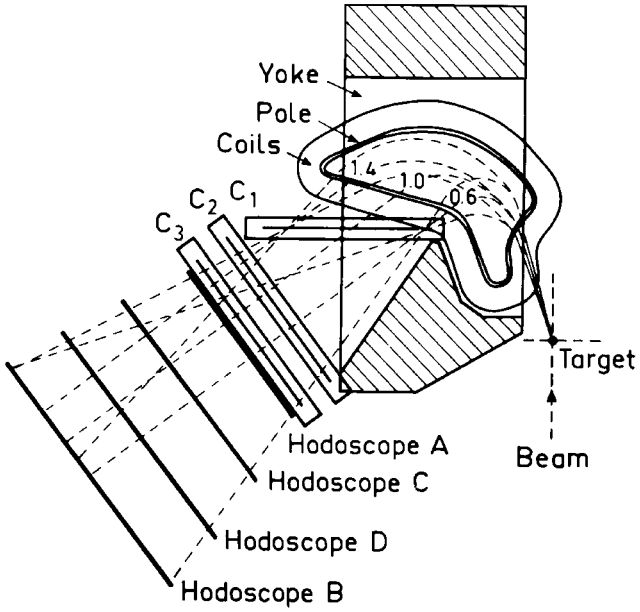

Fig. 1. The SPES3 spectrometer and the associated detection system.

– The missing mass of the $\vec{\mathrm{d}}\mathrm{p} \rightarrow \mathrm{ppX}$ reaction was studied at two incident deuteron energies: $T_{\mathrm{d}} = 1.722$ GeV and 2.1 GeV.

We compare the masses of our structures to the masses of small structures which can be extracted from various reactions studied with incident hadrons or leptons by different collaborations. The observed masses will be discussed in sect. 7 within a phenomenological model based on two quark cluster configurations. Finally, the last part is devoted to conclusions.

2 Experiment

2.1 Experimental description

The measurements were performed at the Saturne synchrotron beam facility. The proton beam energies were 1.52 GeV, 1.805 GeV and 2.1 GeV, and the deuteron beam energies were 1.72 GeV and 2.1 GeV. The particles were detected using the SPES3 spectrometer and detection system (see fig. 1). The main properties of the spectrometer were

– a solid angle of ± 50 mrad in both the horizontal and vertical planes, and
– a large momentum range (600 MeV $< pc <$ 1400 MeV) at $B = 3.07$ T.

The liquid-H_2 target of 393 mg/cm^2 was held in a container with 130 μm thick Ti windows. External heat shields comprised of 24 μm thick aluminium were placed in the beam-line on either side of the target. The number of beam particles per burst varied between 10^8 and 5×10^8, depending on the spectrometer angle and the incident energy. The length of each burst depends on the incident proton energy, and was typically equal to 300 ms. The beam intensity was chosen in such a way that the acquisition dead time was less than 10%. The vertical angular acceptance was determined using the spectrometer magnetic-field map and GEANT code [8]. The drift chambers, the trigger and the acquisition code were designed in order to detect, to identify and to measure the properties of two-particle reactions.

Several drift chambers were used to reconstruct the particle trajectories. The first chamber C1 (called "MIT-type") [9] , was situated on the spectrometer focal plane. Its spatial and angular horizontal resolutions are $\sigma_x = 90$ μm and $\sigma_\theta = 18$ mrad, respectively. Its efficiency was carefully calibrated using the other drift chambers. Two multidrift chambers, C2-C3 (called the "CERN-type" chambers), placed perpendicular to the average particle direction, were designed to get information on trajectories in the horizontal and vertical planes. However, due to the small angular vertical magnification of the spectrometer (≈ 0.14), the ϕ resolution at the target was too poor to be useful.

The trigger consisted of four planes of plastic scintillator hodoscopes. The first and last planes were made of 20 scintillators each. The dimensions of each plastic detector were 12×40 cm^2 for the first plane (A), and 18×80 cm^2 for the last plane (B). The time-of-flight baseline from the first scintillator plane to the last one was 3 m. Particles were identified by their time of flight between the A_i and B_j detectors and also by their energy loss in the A_i detectors. This latter measurement was mainly used to discriminate between simply or doubly charged particles. Mean-timers and constant fraction discriminators were used and the time resolution for each scintillator was typically $\sigma = 180$ ps. The large horizontal angular magnification of the spectrometer produced a large horizontal angular opening (up to 30°) of the trajectories at the output of the spectrometer. This resulted in a large number of useful A_iB_j combinations (125), between the first and last scintillator planes, which required the same number (125) of coincidences. It is important to note that a mean range of ≈ 200 MeV/c (25% of the focal-plane momentum acceptance) is seen by each A_iB_j combination. Therefore, there is a large overlap between many A_iB_j trigger combinations for each spectrometer momentum. The count rate at each momentum value is then less liable to be influenced by errors from the scintillator efficiency. Careful trigger efficiency measurements of all the 125 combinations were performed using a system of small scintillator counters moving in front of the A-hodoscope and behind the B-hodoscope. The mean value of the trigger efficiency was $\approx$ 95%.

When the scattering angle or the incident energy vary, the mean value of the missing mass M_{X} changes for a given A_iB_j coincidence.

2.2 MIT drift chamber efficiency

The MIT drift chamber was located in the focal plane of the spectrometer. It therefore played a major role in our

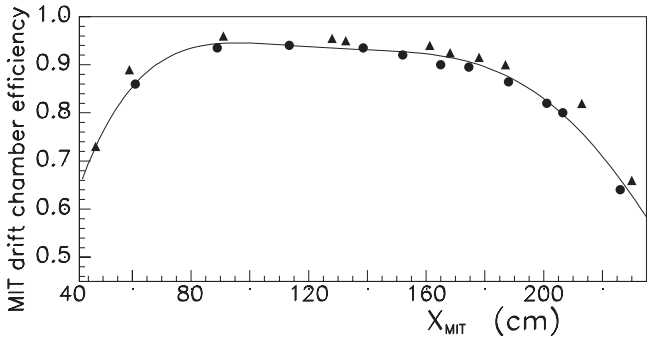

Fig. 2. The MIT drift chamber efficiency. The triangles correspond to the one-particle detection efficiency, whereas the circles correspond to the double-hit detection efficiency.

detection system, justifying a careful efficiency calibration. The efficiency of the MIT drift chamber was evaluated using the CERN drift chambers, by calculating the ratio of the number of times where all three detectors were hit to the number where only the two CERN chambers were hit. Figure 2 shows that this efficiency displays a slowly varying value as a function of position. Consequently this efficiency correction cannot be a source of structures. In fig. 2 the circles correspond to events where two particles were detected, and the triangles to single-particle events. Given the large momentum bite of the spectrometer, the data were taken without having to change the magnetic field. Consequently, the regularly spaced structures seen in the results cannot be attributed to a mis-treatment of the MIT drift chamber efficiency.

2.3 Pion-proton identification

In fig. 3, four typical time-of-flight raw spectra, chosen among the 125 different possibilities, are shown. We observe the quality of the particle identification by looking at the two-peak separation corresponding to pion and proton times of flight. The four inserts correspond to different spectrometer mean momenta and different angles. The inserts (a), (b), (c), and (d) correspond respectively to 1.36 GeV/c (top spectrometer momentum value), 1.25 GeV/c, 1.00 GeV/c, and 0.83 GeV/c. The separation is always very good, even on the high-momentum side.

A second time of flight between both detected particles was used online in order to control the intensity-dependent random hit rate. The same device was also used offline in order to reject the very small amount of badly identified particles between pions and protons at the top of the momentum range (see fig. 3(a)). The time measured was corrected using the particle momenta, the corrections being calculated from the variable distances from the target to the first scintillating plastic hodoscope plane A. After pedestal corrections and variable distance corrections, the time differences of all the A_iA_j time of flights ($20 \times (20-1)/2 = 190$ combinations) were plotted on the same histogram and are shown in fig. 4. We observe a tail due to accidental coincidences to the left of the peak. A window of $\pm$ 9 channels, as drawn in the

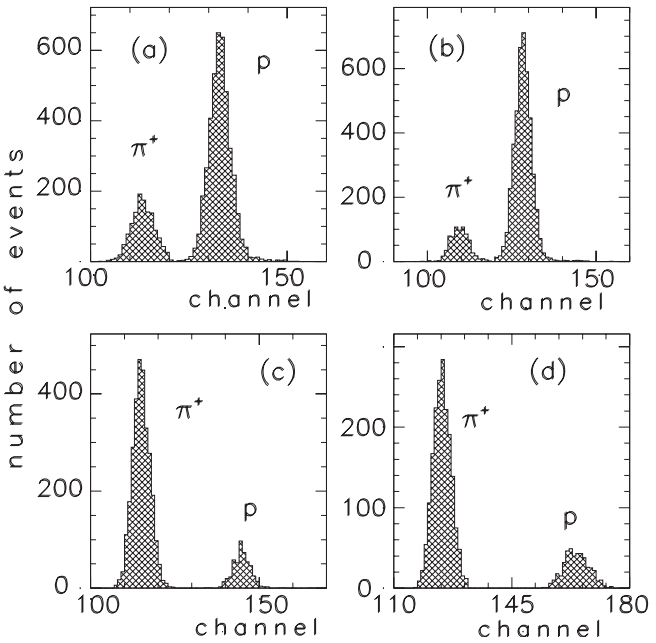

Fig. 3. Time-of-flight spectra for four A_iB_j combinations consisting of the number of events *versus* the channel number (125 ps/channel). The four inserts (a), (b), (c), and (d) correspond respectively to the following mean momenta: 1.36 GeV/c, 1.25 GeV/c, 1.00 GeV/c, and 0.83 GeV/c.

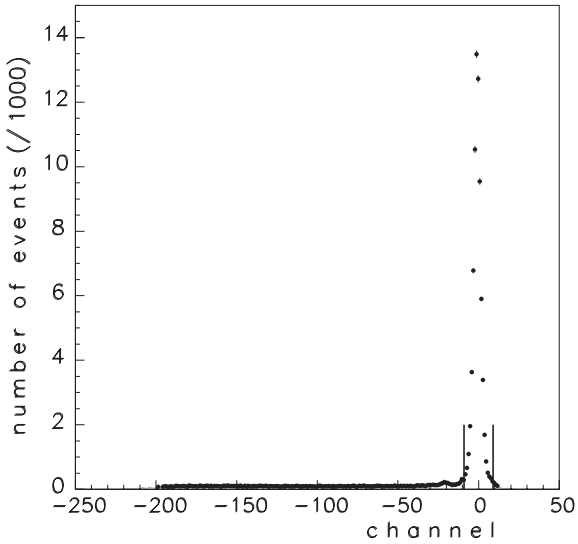

Fig. 4. Spectra of the second time of flight comprised of the number of events *versus* the channel number (250 ps/channel) for all 190 A_iA_j combinations (see text) of the pp $\rightarrow$ ppX reaction at $T_{\rm p} = 2.1$ GeV and $\theta = 3^\circ$.

figure, was used in the detailed data analysis. Incorrect proton-pion identifications fell around channel -21, and can be seen as a small peak in the figure. These badly identified proton-pion events correspond to events that lie in the tail crossovers of the particle identification at the top end of the momentum scale (see fig. 3(a)). The spectra of the first time of flight (fig. 3) were vetoed by the second time of flight.

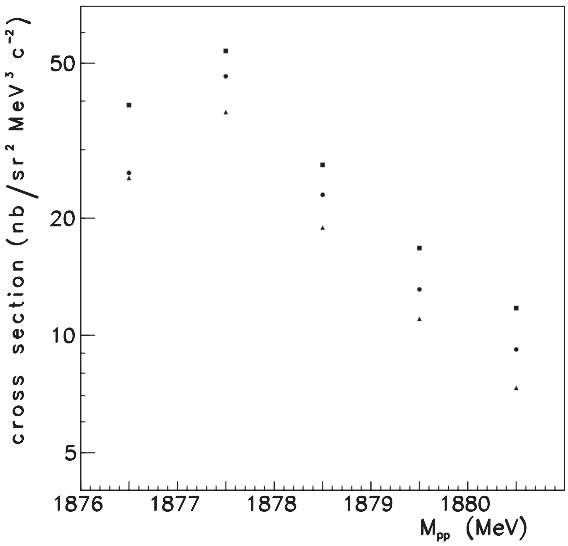

Fig. 5. Invariant mass of the pp FSI peaks from the pp → ppX reaction. Full circles, squares, and triangles correspond, respectively, to data obtained at $T_{\rm p}$ = 1.52 GeV, 1.805 GeV, and 2.1 GeV. The 2.1 GeV cross-sections are vertically shifted by $-2\,{\rm nb/sr^2MeV^3}c^{-2}$ to distinguish the data.

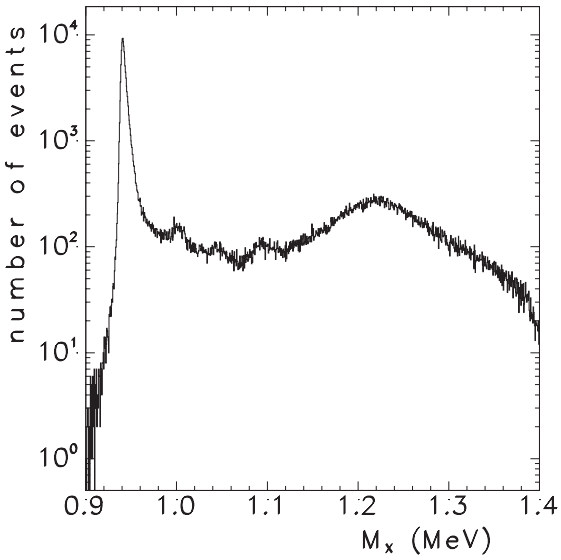

Fig. 6. Missing-mass spectrum for the pp → pπ^+X reaction at $T_{\rm p}$ = 1.805 GeV and $\theta = 0.75°$.

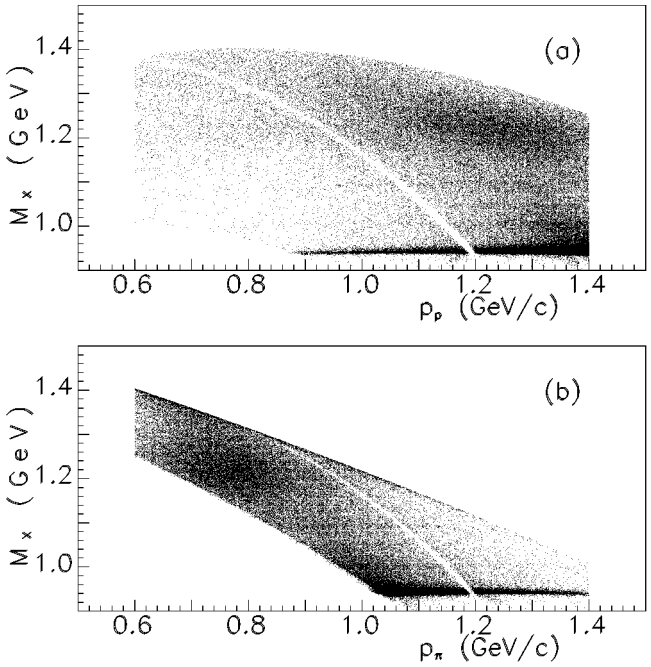

Fig. 7. Scatter plot of the missing mass *versus* the proton momenta (insert (a)), and the missing mass *versus* the pion momenta (insert (b)) from the pp → pπ^+X reaction at $T_{\rm p}$ = 1.805 GeV and $\theta = 0.75°$.

2.4 Resolution

An important property of the experiment is the good resolution, essential when narrow and weakly excited structures are being looked for. The resolution in the invariant mass was measured using the final-state interaction peak (FSI) from the pp → ppX reaction. Figure 5 shows these distributions for all three energies. Here, full circles, squares, and triangles correspond respectively to results from $T_{\rm p}$ = 1.52 GeV, 1.805 GeV, and 2.1 GeV incident energies. The total experimental resolution is $\sigma \approx 0.9$ MeV.

The resolution of the missing mass was measured in the neutron missing mass from the pp → pπ^+X reaction at forward angles. Figure 6 shows the missing-mass spectrum, on a logarithmic scale, when the incident proton beam was $T_{\rm p}$ = 1.805 GeV and the spectrometer angle $\theta = 0.75°$. Here, the experimental resolution is $\sigma \approx 2.2$ MeV. The resolution of the missing mass lowers for increasing angles.

We clearly see three structures in fig. 6, between the neutron peak and the Δ bump. They are unexpected since there is no room for new low-mass and narrow baryons within the many-quark models [10]. Many checks were performed to ascertain the real presence of these new physical structures and they will be discussed in detail in sect. 5.

3 Cross-section determination

Several normalizations were performed in order to extract the cross-sections and several corrections were applied which take into account accidental coincidences, lost events, angular vertical acceptances, and drift chamber and trigger efficiencies. The beam flux was calibrated with the help of two telescopes in direct view of the target and an ionisation chamber downstream of the beam. These three detectors were calibrated using ^{12}C activation measurements. The data were also normalized to the two detected-particle momenta ranges. Indeed these momenta acceptances vary for different missing masses (or invariant masses), different reactions, spectrometer angles and different incident energies. Figure 7 shows these variations for the missing mass of the pp → pπ^+X reaction at $T_{\rm p}$ = 1.805 GeV and $\theta = 0.75°$. This normalization was done for all cross-sections presented. The momenta acceptances were obtained from analytical relations or

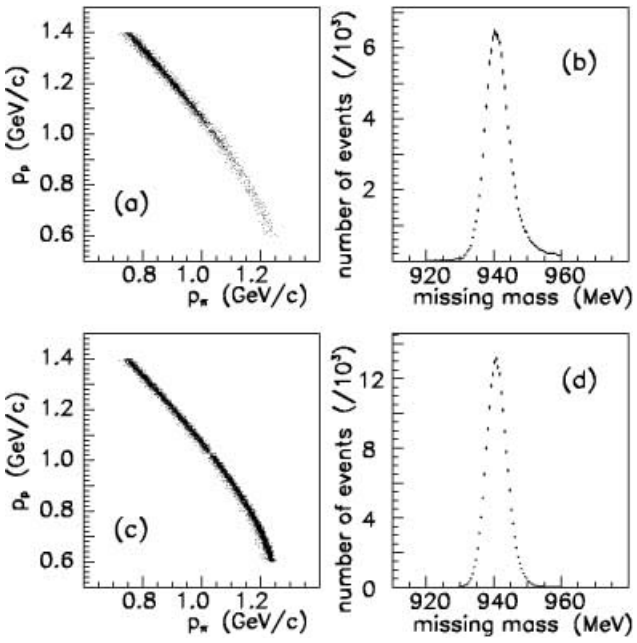

Fig. 8. Neutron missing-mass peak from the $pp \rightarrow p\pi^+X$ reaction at $T_p = 1.52$ GeV, $\theta = 0°$. Inserts (a) and (b) correspond to data, inserts (c) and (d) are from simulation.

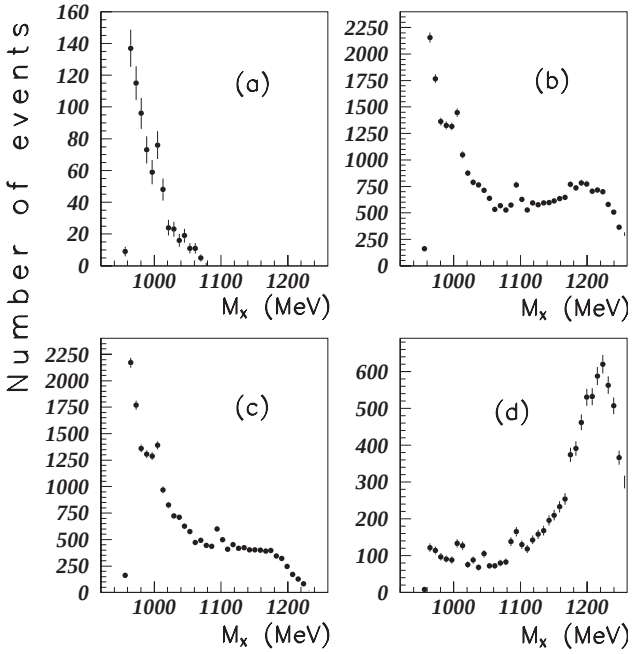

Fig. 9. The $pp \rightarrow p\pi^+X$ reaction at $T_p = 1.52$ GeV and $\theta = 0°$. Selection of several momenta ranges in inserts (a), (b), (c), and (d), respectively: $p_\pi \geq 1$ GeV/c, $p_\pi \leq 1$ GeV/c, $p_p \geq 1$ GeV/c, and $p_p \leq 1$ GeV/c.

numerical fits to real or simulated data (see later in sect. 5.1). We have checked that the same final cross-sections were obtained independently of the choice made for this normalization. The empty line in the figure will be discussed in the next paragraph.

4 Simulation

A simulation code was written in order to study the properties of the spectrometer and detectors. All experimental parameters were found to be well understood, and no narrow structures are observed in the simulated histograms. The simulation allows us to evaluate the corrections for the lost events. Vertical angular acceptance corrections were previously determined with GEANT. The main events lost are those where both particles detected have the same momentum. These events define a narrow empty valley that can be seen clearly in fig. 7. Such a small region, where important losses occur, is without consequence when M_X from $pp \rightarrow p\pi^+X$ is considered, but important for a narrow region in $M_{p\pi^+}$ (mainly for neutron missing masses). This region of invariant mass was eliminated from further consideration in order to avoid the introduction of fake structures via a substantial renormalization.

Figure 8 shows a comparison between the neutron missing-mass data and the corresponding simulation for the $pp \rightarrow p\pi^+X$ reaction at $T_p = 1.52$ GeV and $\theta = 0°$. Inserts (a) and (b) show data, whereas inserts (c) and (d) show the corresponding simulated results. Inserts (a) and (c) show that these events came from the total momentum range ($0.6 \leq pc \leq 1.4$ GeV). Both neutron missing-mass peaks are shown in inserts (b) and (d). They are regular and do not display any internal structures. Had there been dead wires in the detectors, we would have expected regions of varying density. This is not observed. There is no evidence either of the opposite situation of self-excited wire amplifiers. In fig. 8 the cross-section variation for $pp \rightarrow p\pi^+n$ which differs between data and simulation, explains the difference in intensity between inserts (a) and (c).

5 Checks

A careful internal calibration of all elements was undertaken, and all possible cross-checks were carried out in order to evaluate the level of confidence that can be attributed to the existence of the observed structures. In the following we provide the description of the procedures used.

5.1 Selection of different momenta ranges

Several tests were performed in order to verify that the structures were not produced in a limited region of momenta. The data from the $pp \rightarrow p\pi^+X$ reaction at $T_p = 1.52$ GeV and forward angles were used. The neutron peak was removed by software cuts in order to enhance the missing-mass region of interest. The statistics are consequently reduced in figs. 9, 10, and 11 [11]. It will be seen later, in fig. 29, that the structure at $M = 1044$ MeV is weakly excited at $T_p = 1.52$ GeV. This is also observed in figs. 9 and 10, which contain data that are also parts

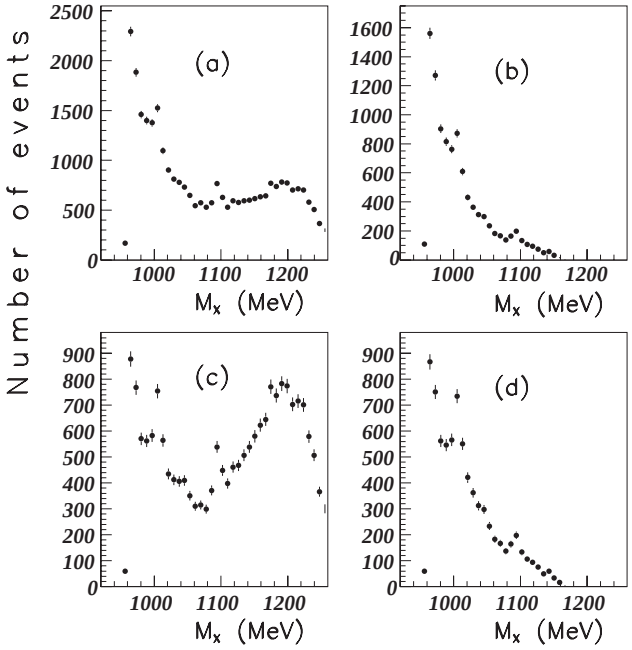

Fig. 10. Missing mass of the pp → pπ^+X reaction at T_p = 1.52 GeV and $\theta = 2°$. The four inserts (a), (b), (c), and (d) correspond to events selected by software analysis cuts in the following momenta ranges $0.6 \leq pc \leq 1.4$ GeV (total range), $0.8 \leq pc \leq 1.4$ GeV, $0.6 \leq pc \leq 1.2$ GeV, and $0.8 \leq pc \leq 1.2$ GeV, respectively.

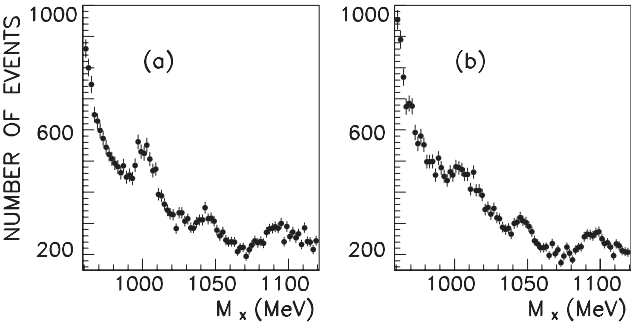

Fig. 11. Missing mass of the pp → pπ^+X reaction at T_p = 1.805 GeV. In both inserts (a) and (b), a selection on detected-particle momenta is made in order to keep only momenta where one of the detected particles has $p \geq 1.2$ GeV/c. Both inserts (a) and (b) correspond to $\theta = 0.75°$ and $\theta = 3.7°$ measurements, respectively.

of the data of fig. 29 below. At both extremities of the momenta, the trajectories' envelope fits exactly the trigger dimensions. Therefore cuts selecting these momentum extremities were also performed. Figure 7 shows that there is no event for $M_X \leq 1100$ MeV, if $p_\pi \leq 840$ MeV/c. There are also very few events if $p_p \leq 840$ MeV/c. This is not only true for $T_p = 1805$ MeV data, but nearly the same situation occurs for $T_p = 1520$ MeV data. Therefore the check is only performed using soft cuts in the range $p \geq 1.2$ GeV/c. Figure 11 shows the results of such cut applied on the $T_p = 1.805$ GeV data, at respectively

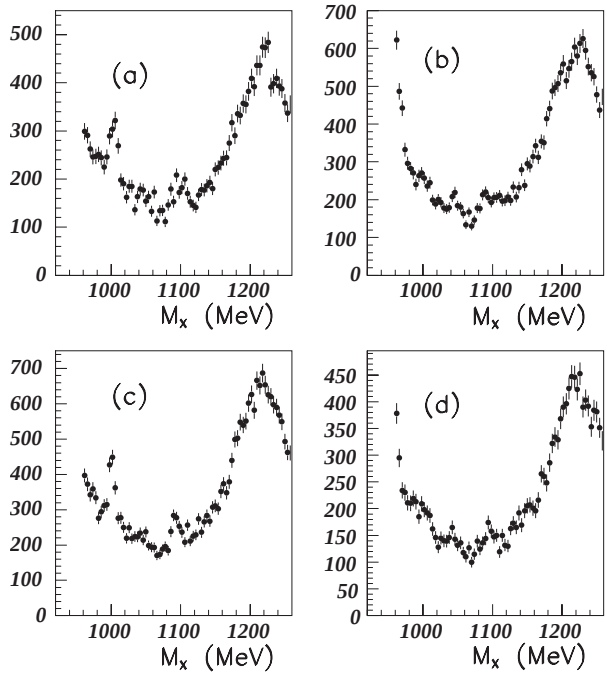

Fig. 12. Missing mass of the pp → pπ^+X reaction at T_p = 1.805 GeV, $\theta = 0.75°$. The four inserts (a), (b), (c), and (d) correspond to events selected by software cuts in the following angular ranges, respectively: $\theta_p \geq 0°$ and $\theta_{\pi^+} \geq 0°$, $\theta_p \leq 0°$ and $\theta_{\pi^+} \leq 0°$, $\theta_p \geq 0°$ and $\theta_{\pi^+} \leq 0°$, and $\theta_p \leq 0°$ and $\theta_{\pi^+} \geq 0°$. Here, the range is defined around the mean horizontal direction of the spectrometer aperture.

$\theta = 0.75°$ (insert (a)) and $\theta = 3.7°$ (insert (b)). We observe that the structures remain.

5.2 Selection of different angular ranges

Different angular cuts were performed during the analysis in order to test that our structures remain for different angular ranges inside our horizontal aperture of ±50 mrad. Figure 12 shows that is indeed the case. The data of the pp → pπ^+X reaction at $T_p = 1.805$ GeV and $\theta = 0.75°$ are presented in four different angular ranges. Here, the range is defined around the mean horizontal direction of the spectrometer aperture. Although the three structures are present in all four inserts, their relative excitation differs. The structure at $M = 1094$ MeV is important in the four parts of the figure. The structure at $M = 1004$ MeV is weak in the second part of fig. 12, insert (b), when both particles are detected in the negative part of the horizontal spectrometer aperture. It is however still present. The results of the same angular cuts applied by software on the data obtained at $T_p = 1.805$ GeV and $\theta = 3.7°$ are presented in fig. 13. We observe that all three structures are present in all four angular selections, except perhaps in insert (b) where the data in the 1044 MeV region does not show a stable behaviour.

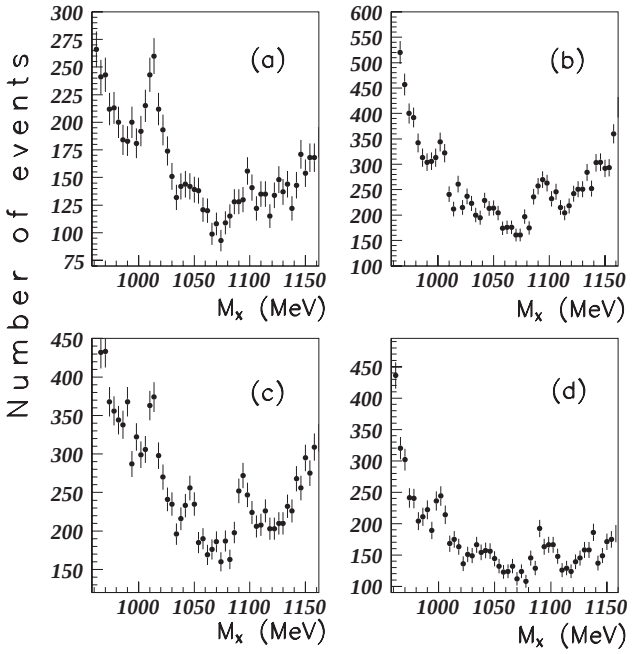

Fig. 13. Missing mass of the pp $\rightarrow$ pπ^+X reaction at $T_\mathrm{p} = 1.805$ GeV, $\theta = 3.7°$. The same angular selections as in fig. 12 are performed in inserts (a), (b), (c), and (d).

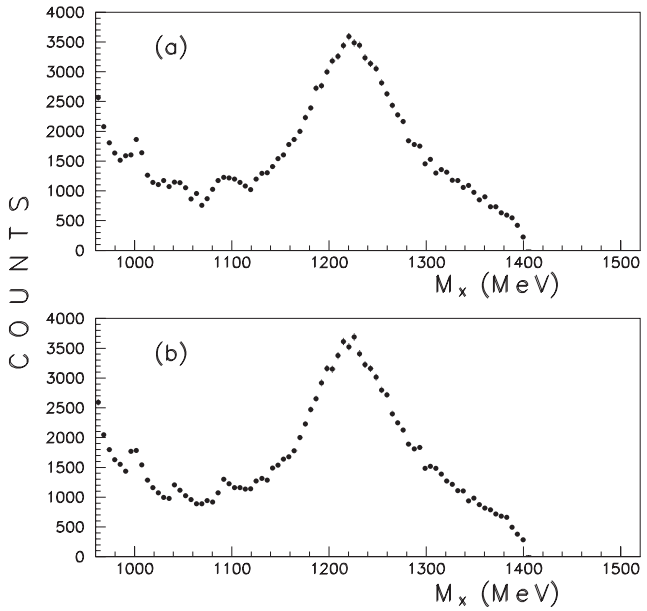

Fig. 14. Missing mass of the pp $\rightarrow$ pπ^+X reaction at $T_\mathrm{p} = 1.805$ GeV and $\theta = 0.75°$. Inserts (a) and (b) correspond to both spin states of the incident proton beam.

5.3 The structures do not depend on the spin state of the incident beam

Figure 14 shows the missing mass of the $\vec{\mathrm{p}}\mathrm{p} \rightarrow \mathrm{p}\pi^+\mathrm{X}$ reaction at $T_\mathrm{p} = 1.805$ GeV and $\theta = 0.75°$. The inserts (a) and (b) correspond to the two spin states of the incident particles. We observe that the structures are present in both cases.

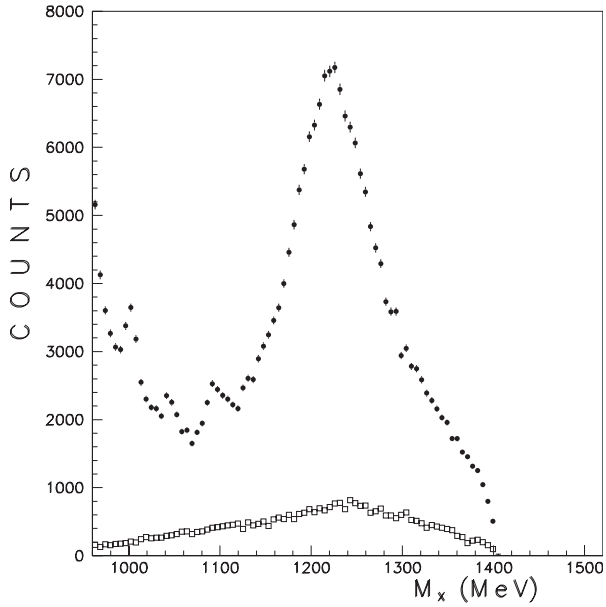

Fig. 15. Missing mass of the pp $\rightarrow$ pπ^+X reaction at $T_\mathrm{p} = 1.805$ GeV and $\theta = 0.75°$. True coincidences (full circles) are compared to random coincidences (empty squares) defined over a range 12 times greater.

5.4 Structures not present in accidental coincidences

Figure 15 shows the comparison between the real events and the accidental coincidences of the missing mass from the pp $\rightarrow$ pπ^+X reaction at $T_\mathrm{p} = 1.805$ GeV and $\theta = 0.75°$. The accidental coincidences are defined by software cuts in a time range 12 times larger than the true p-π^+ coincidences. The corresponding histogram does not display any structure.

5.5 Empty target measurements

The effect of the target windows was checked on the same cell, by regular empty target measurements performed during the data taking. The count rates were always small. Figure 16 shows one comparison of full target to empty target measurements. The missing-mass data from the pp $\rightarrow$ pπ^+X reaction at $T_\mathrm{p} = 1.805$ GeV and $\theta = 0.75°$ are presented. Here, both spectra correspond to the same incident proton flux. We observe the absence of structures in the empty target data. We deduced that the target windows were not a source of a noticeable contamination. We also deduced that although our measurements were performed at small angles, the data were not contaminated by any hot area of incident beam which could have been scattered by some mechanical element at the entrance of the spectrometer.

5.6 Possible inefficient or hot wire in the MIT chamber

As already said the efficiency of all elements of the detection system was calibrated. However it is possible to

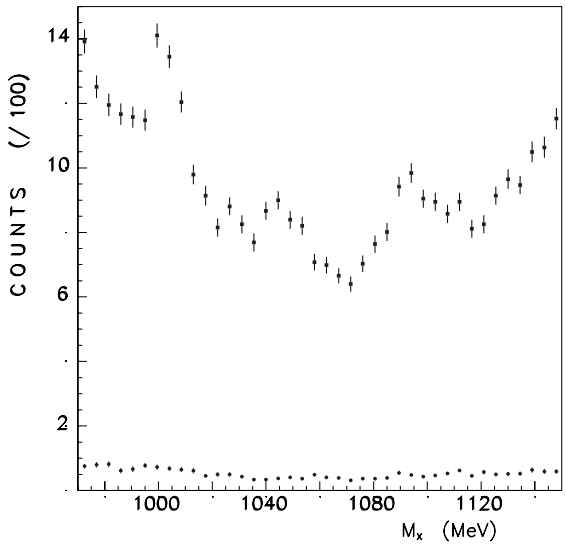

Fig. 16. Missing mass of the pp $\rightarrow$ pπ^+X reaction at $T_\mathrm{p} = 1.805$ GeV and $\theta = 0.75°$. Comparison of full (squares) and empty (circles) target data, normalized to the same incident proton beam flux.

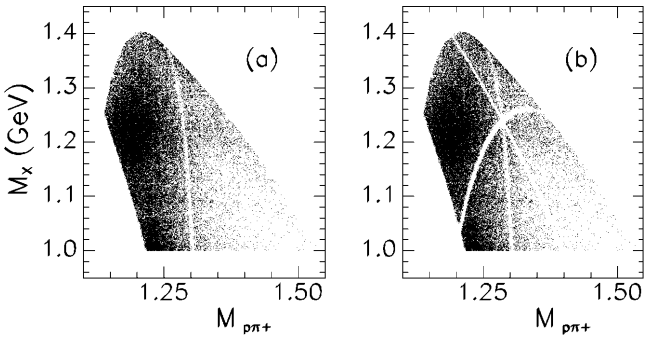

Fig. 17. Scatterplot of missing mass M_X *versus* invariant mass $M_{\mathrm{p}\pi+}$ from the pp $\rightarrow$ pπ^+X reaction at $T_\mathrm{p} = 1.805$ GeV and $\theta = 0.75°$. Both parts show the data where the events with $M_\mathrm{X} \leq 1$ GeV were subject to software cuts in order to remove the intense neutron peak. Part (b) shows the same events after removal of particles having a momentum $900 \leq p \leq 920$ MeV/c.

give additional arguments allowing to exclude possible inefficient or hot wires in the MIT chamber. All final data (missing masses or invariant masses) were the results of two-particle detection. Any possible inefficient or hot wire in the MIT chamber will affect both particles. The consequence will be a weak or intense narrow vertical range in both parts of fig. 7. Indeed, 3 to 5 wires are hit for each trajectory. The figures showing the scatterplot of p_p *versus* p_{π^+} events will display a weak or intense cross. The figures showing the scatterplot of M_X *versus* $M_{\mathrm{p}\pi^+}$ events will dispay weak or intense bent lines neither parallel to the M_X axis, nor parallel to the $M_{\mathrm{p}\pi^+}$ axis. This effect is illustrated in fig. 17 for $T_\mathrm{p} = 1805$ MeV events, $\theta = 0.75°$. Both parts show the data, with software cuts for $M_\mathrm{X} \leq 1$ GeV in order to remove the intense neutron peak. Part (b) shows the same events after removal of particles having a momentum $900 \leq p \leq 920$ MeV/c. Such weak or intense bent curves were never observed in the data. Anyway, the projection of any such weak or intense line would never produce a peak or trough, either in M_X spectra, or in $M_{\mathrm{p}\pi^+}$ spectra.

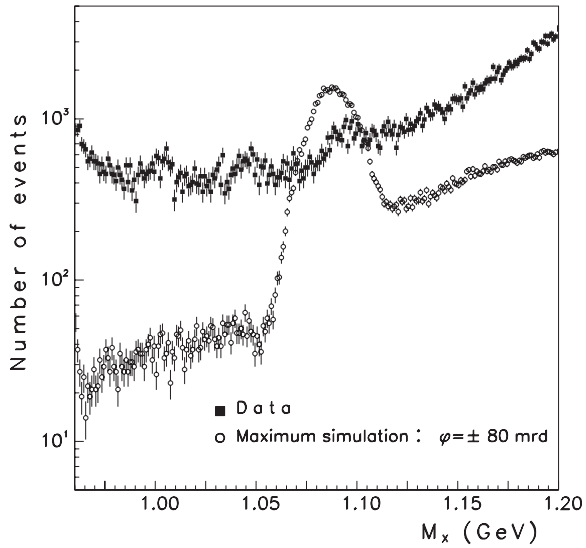

Fig. 18. Effect of a possible slowing-down of p and π^+ through lead slits and stainless steel rings at the entrance of the spectrometer. pp $\rightarrow$ pπ^+X reaction at $T_\mathrm{p} = 2.1$ GeV and $\theta = 0.7°$. Squares correspond to data, whereas circles correspond to simulated slower particles, normalized by the same neutron missing-mass peak.

As already said, every trigger scintillator corresponds to a large momentum range, and also will concern both detected particles. Consequently, it is deduced that any inefficiency or hot point in any detector is unable to produce a narrow peak.

5.7 Possible effect of particles emitted outside the spectrometer solid angle and slowed down

We consider here the possibilty to attribute the narrow structures to a possible slowing-down of the detected particles (p and-or π^+) corresponding to the pp $\rightarrow$ pπ^+n reaction. The particles could be emitted outside the solid angle and then could be partially absorbed by the lead diaphragm and-or other mechanical elements at the entrance of the spectrometer. A careful simulation of this possible effect was performed. There is no ambiguity in the horizontal plane. But, since the vertical angular magnification of the spectrometer is small, the drift chambers were not precise enough to make clear vertical cuts. The spectrometer aperture is ± 50 mrad. Trajectories emitted vertically up to ± 80 mrad were simulated and particles emitted with momenta up to 2 GeV/c were studied (the maximum detection momentum is 1.4 GeV/c). Figure 18 shows the result of the simulation normalized to the missing mass of the neutron peak (logarithmic scale). There are no obvious peaks due to such effect in the range outside $1.06 \leq M_\mathrm{X} \leq 1.11$ GeV for the missing mass of the

pp $\rightarrow$ pπ^+X reaction at $T_\mathrm{p} = 2.1$ GeV and $\theta = 0.7°$. A similar result was found [12] for a comparable simulation performed under different experimental conditions, namely the pp $\rightarrow$ pπ^+X reaction at $T_\mathrm{p} = 1.805$ GeV and $\theta = 0.75°$. A broad peak is observed inside the range $1.06 \leq M_\mathrm{X} \leq 1.11$ GeV and could correspond to possible fake events slowed down by the lead diaphragm.

Trajectories for increasing angles ($|\Delta\ \phi| \geq 50$ mrad) are progressively cut by the magnet, the yoke and the detectors. For the detectors, this is particularly true at both extremities, since the trajectories' envelopes fit exactly the trigger dimensions, which correspond to $\Delta\phi = \pm 50$ mrad. Figure 11 illustrates clearly the presence of structures in these extreme momentum regions, where the fake effect discussed here cannot be present.

There are additionnal arguments excluding this effect which could attribute the narrow structures to particles slowed down by the slits. If the structures were produced by the neutron peak shadows, then:

- for increasing spectrometer angles, the simulation shows that
  - the mass of the broad fake peak would increase (up to 20 MeV),
  - its width would increase (up to 75 MeV);
- the ratio of the cross-sections of the structures *versus* the neutron missing-mass cross-sections should be flat;
- the analyzing powers of the structures and of the neutron missing-mass peak should always be equal.

None of these characteristics are observed. We concluded, therefore, that this type of contamination was not present.

6 Results

All the checks described till now lead us to conclude that genuine structures are observed. Each corresponding mass and width was obtained using a polynomial distribution for the background and a Gaussian one for the peak. The precision of the extracted peaks was determined by the corresponding number of standard deviations (SD):

$$\mathrm{SD} = 1/\sqrt{2}\sum_{i=1}^{n}\left[(N_{Ti}-N_{Bi})/\Delta\sigma_i^2\right] \Big/ \left[\sum_{i=1}^{n}(1/\Delta\sigma_i^2)\right]^{1/2} \quad (1)$$

where the sum is taken over the n different channels describing the peak. N_T and N_B describe the total and background count rates of each channel, $\Delta\sigma_i$ is the corresponding statistical error and the factor $1/\sqrt{2}$ comes from the assumption that the error on N_B is the same as the error on N_T.

The next step in the analysis is to try to understand the origin of these structures and how they may be related. The main point will be to see if, whether or not, they appear at stable masses. The answer will be given after looking at the different results.

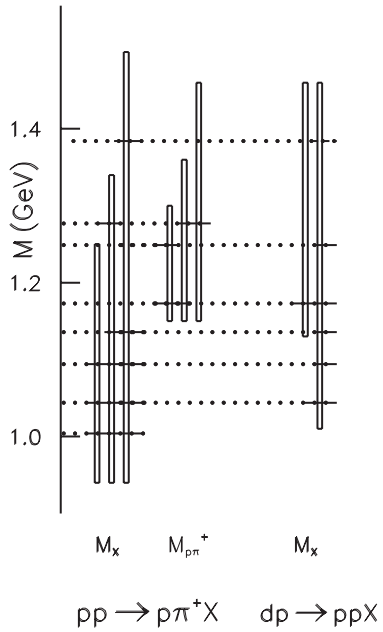

Fig. 19. Range of baryonic masses studied in different reactions. The narrow strips correspond to the different incident energies (increasing from left to right for each observed variable and each reaction). The horizontal lines indicate the masses of the observed narrow structures.

6.1 Ranges of baryonic mass studied by different reactions

Figure 19 shows the useful range of baryonic missing masses studied below $M = 1.46$ GeV. The three (two) narrow strips for each reaction correspond to the three (two) different incident energies, increasing from left to right, for the reactions studied. The variations of these limits for different spectrometer angles are small and therefore not pointed out. The statistics are not regularly distributed. At both sides of each range the statistics are poor, therefore narrow structures could exist in these cases, and have not been extracted in this study. The horizontal lines indicate the mass of the observed narrow structures to be discussed in the following paragraphs.

It is sometimes possible to observe small shoulders, or peaks, in publications of data obtained from various reactions studied for different aims. The corresponding experimental resolutions are usually lower than in our experiment. These shoulders or peaks are generally not commented on by the authors. In a few cases they are assumed (without calculation) to be the rescattering of particles in the final state. The cross-sections of the np $\rightarrow$ pX reaction, measured at 0° at nine incident energies at LAMPF [13], exhibit several structures. In this publication a peak can be observed (at $T_\mathrm{n} = 673$ MeV, *i.e.* $M_\mathrm{X} \approx 1136$ MeV and $\sigma \approx 10$ MeV). Other data exist without peaks or shoulders in the mass range studied in the present work. In the spectra of the reaction ep $\rightarrow$ e$'\pi^+X^0$ recently studied [14] at JLAB (Hall A), no significant signal was observed in the range $0.97 \leq M_{\mathrm{X}^0} \leq 1.06$ GeV.

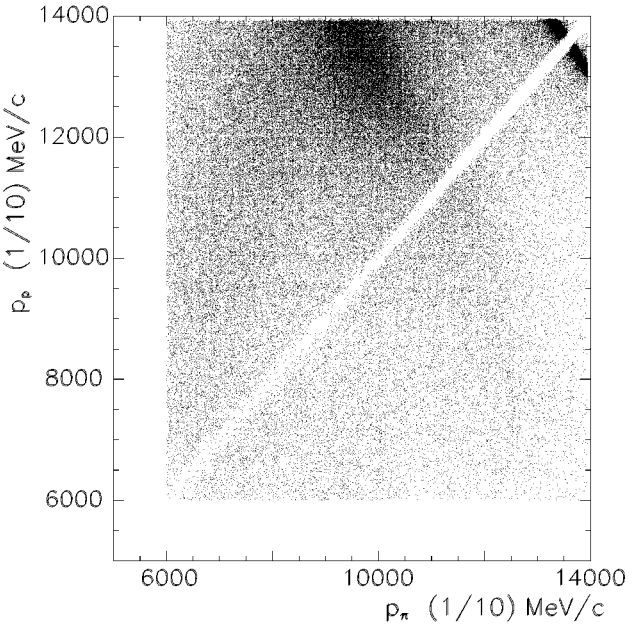

Fig. 20. Scatterplot of p_{p} *versus* $p_{\pi+}$ events from the pp $\rightarrow$ pπ^+X reaction at $T_{\mathrm{p}} = 2.1$ GeV and $\theta = 0.7°$.

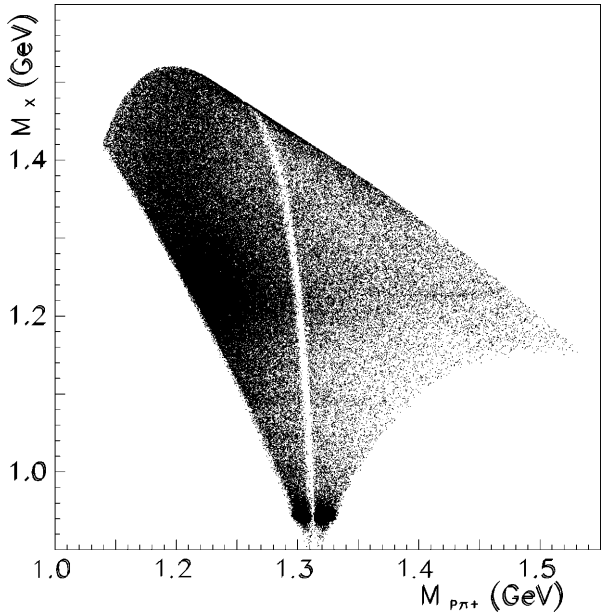

Fig. 21. Scatterplot of missing mass M_{X} *versus* invariant mass $M_{\mathrm{p}\pi+}$ from the pp $\rightarrow$ pπ^+X reaction at $T_{\mathrm{p}} = 2.1$ GeV and $\theta = 0.7°$.

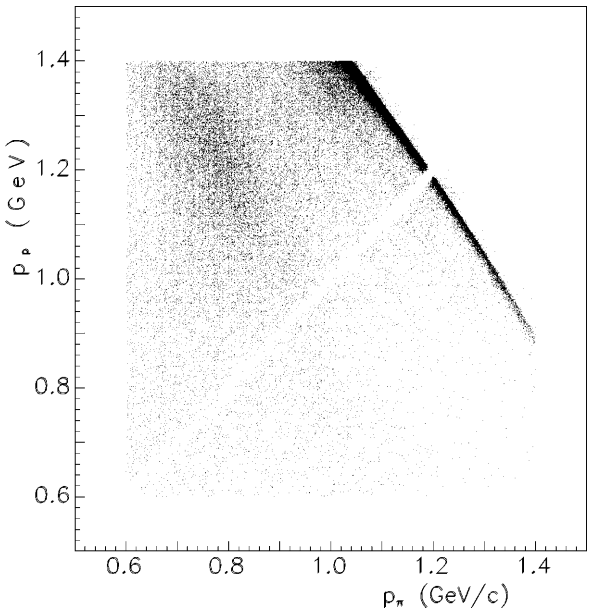

Fig. 22. Scatterplot of p_{p} *versus* $p_{\pi+}$ from the pp $\rightarrow$ pπ^+X reaction at $T_{\mathrm{p}} = 1.805$ GeV and $\theta = 0.75°$.

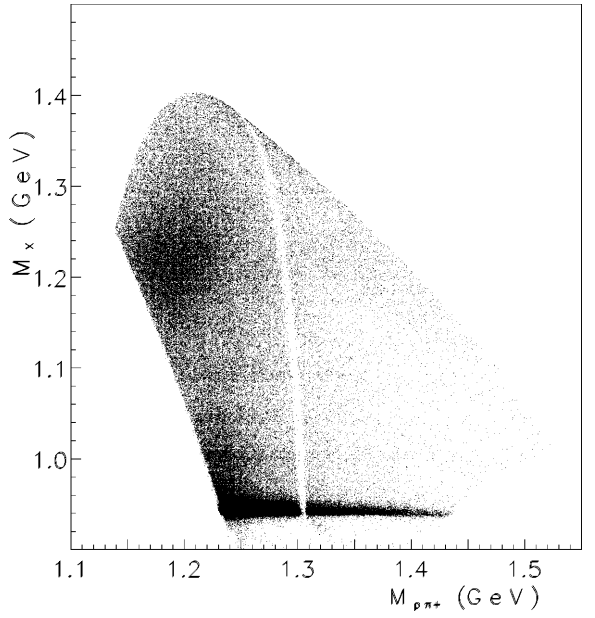

Fig. 23. Scatterplot of the missing mass M_{X} *versus* the invariant mass $M_{\mathrm{p}\pi+}$ from the pp $\rightarrow$ pπ^+X reaction at $T_{\mathrm{p}} = 1.805$ GeV and $\theta = 0.75°$.

Some other results will be discussed later in sects. 6.5, 6.6 and 6.7, and their data will be shown.

6.2 The missing mass of the pp $\rightarrow$ pπ^+X reaction

The first results from this reaction were already published [3,12]. Figure 20 shows the scatterplot of proton momenta against pion momenta from $T_{\mathrm{p}} = 2.1$ GeV and $\theta = 0.7°$ events. The same events, after kinematical transformations, are shown in fig. 21 where the missing mass M_{X} is plotted *versus* the invariant $M_{\mathrm{p}\pi+}$ mass. In both figures, we see clearly the neutron missing mass and the intense broad Δ region. Several narrow lines can be perceived at fixed missing masses between the neutron and Δ missing masses. The empty narrow band, as already explained in sect. 4, corresponds to lost events where both the p and π^+ have the same momentum. Figures 22 and 23 show the corresponding data at lower energy: $T_{\mathrm{p}} = 1.805$ GeV and $\theta = 0.75°$. The data in fig. 23, projected onto the missing-mass axis, are shown in fig. 6. We see clearly the neutron and the Δ peaks, and also small

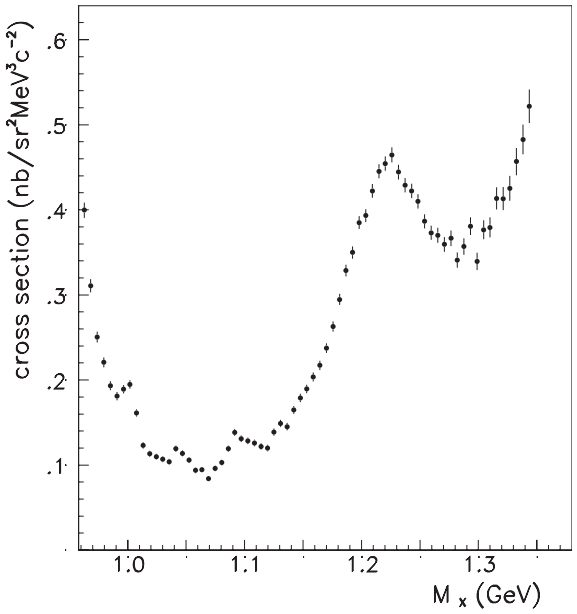

Fig. 24. Cross-section of the missing mass of the pp → pπ^+X reaction at $T_\mathrm{p} = 1.805$ GeV and $\theta = 0.75°$.

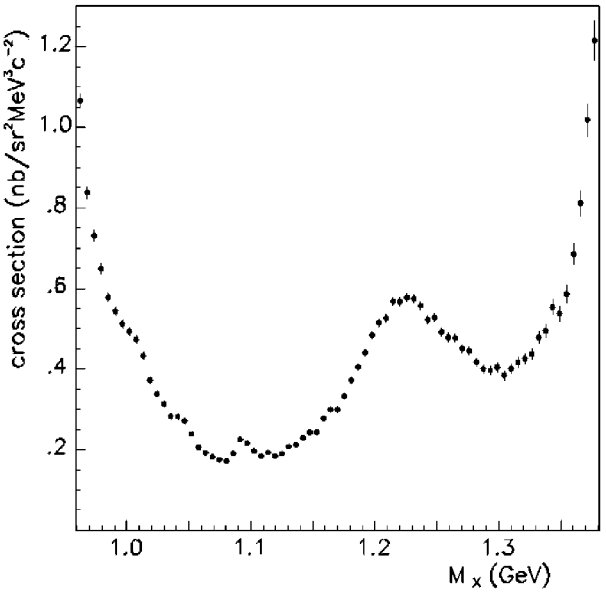

Fig. 25. Cross-section of the missing mass of the pp → pπ^+X reaction at $T_\mathrm{p} = 1.805$ GeV and $\theta = 3.7°$.

structures between the two. In order to enhance these structures, we remove the neutron peak by applying software cuts. Figure 24 shows the result for the pp → pπ^+X reaction at $T_\mathrm{p} = 1.805$ GeV and $\theta = 0.75°$ after this selection, whereas fig. 25 shows the cross-section at the same energy but for $\theta = 3.7°$. A good definition of the structures with respect to the background is obtained.

In order to show the kinematic dependencies of these resonances, we show in figs. 26, 27, and 28 the histograms of the number of events for the three incident energies. At each energy, the large angles are removed, since the

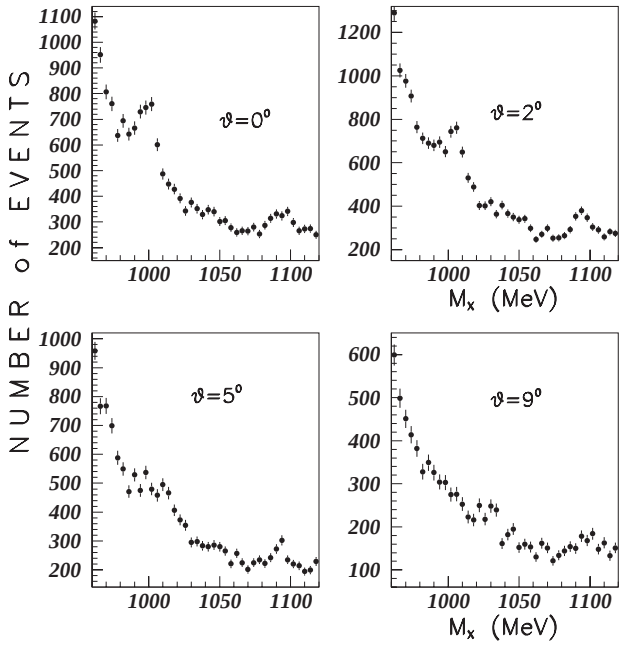

Fig. 26. Number of events *versus* the missing mass from the pp → pπ^+X reaction at $T_\mathrm{p} = 1.520$ GeV and small angles.

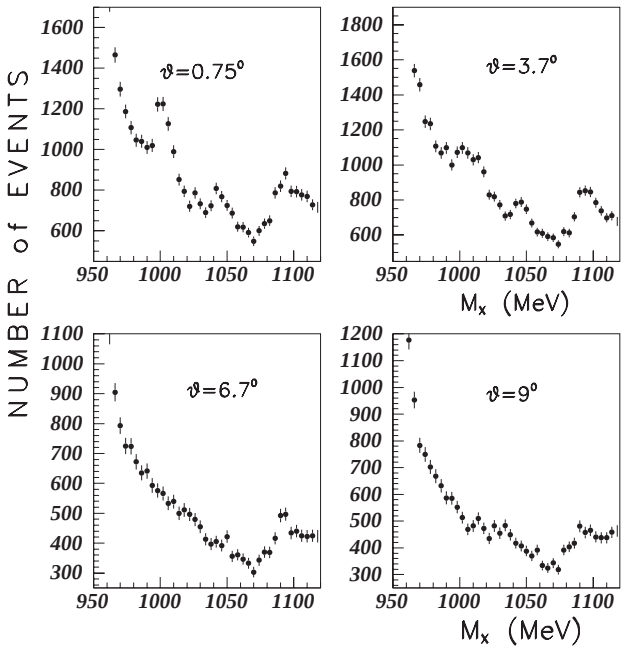

Fig. 27. Number of events *versus* the missing mass from the pp → pπ^+X reaction at $T_\mathrm{p} = 1.805$ GeV and small angles.

statistics and resolution are insufficient. We observe that the first structure at all three energies is strongly excited at small angles, and that its excitation decreases with increasing angle. Its relative excitation remains more or less constant for different energies. The intermediate mass structure excitation decreases also with increasing angle, but its excitation increases with increasing energy. The excitation of the larger mass structure is stable for different angles at a given energy, but increases with increasing

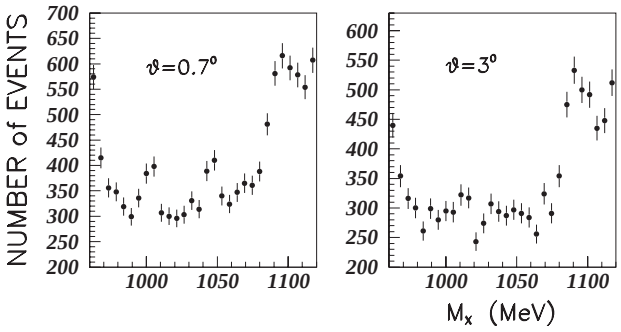

Fig. 28. Number of events *versus* the missing mass from the $pp \rightarrow p\pi^+X$ reaction at $T_p = 2.100$ GeV and small angles.

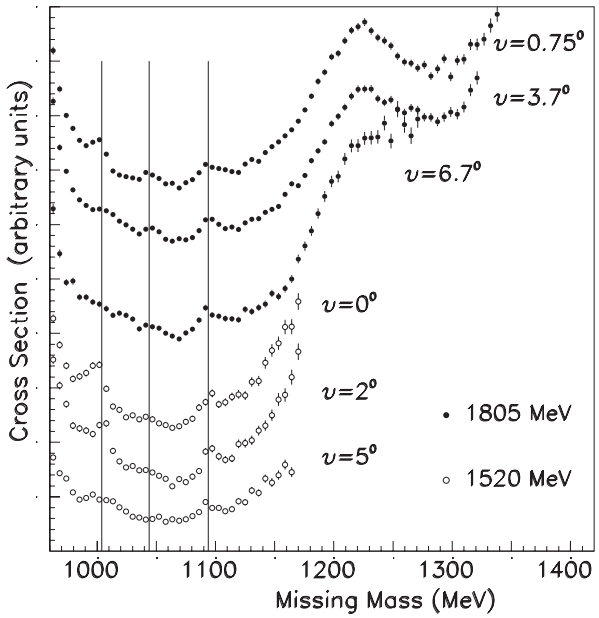

Fig. 29. Missing mass spectra of the $pp \rightarrow p\pi^+X$ reaction at $T_p = 1520$ MeV and 1805 MeV and at the three smallest angles for both energies.

energy. These three different behaviours can be considered as being an additional argument in favour of genuine physical structures.

For these structures to have any meaning we would expect them to appear at the same masses, independently of the spectrometer angle and independently of the incident energy. In order to see if this is true, the cross-sections as a function of missing mass, are shown in figs. 29 and 30 for different forward angles and at all three proton beam energies. The different results are arbitrarily separated by a vertical translation to allow a better observation. In both figures the vertical straight lines are drawn at the same masses. It is observed that the structures are present in many spectra, and when present, are observed at fixed masses: 1004 MeV, 1044 MeV, and 1094 MeV. The associated number of standard deviations (SD) varies between 2 and 16.9. They were previously reported along with the experimental widths [3]. The mass of the first two structures is $M \leq M_N + M_{\pi^+}$. It is impossible to extract the widths of these structures since they are expected to be

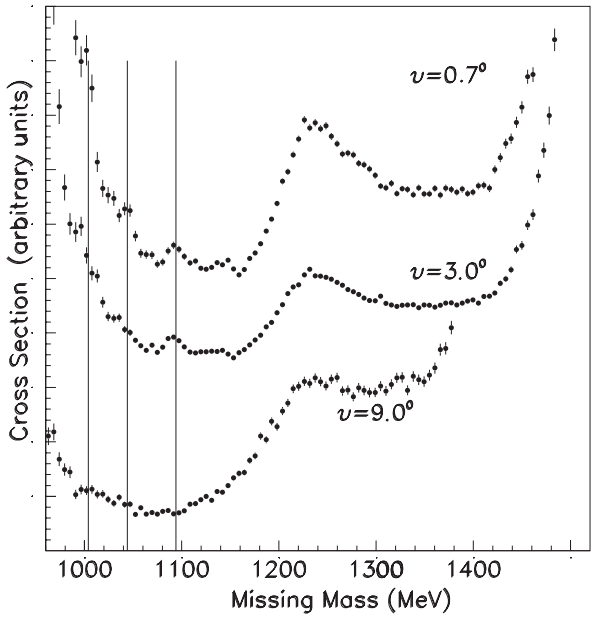

Fig. 30. Missing-mass spectra of the $pp \rightarrow p\pi^+X$ reaction at $T_p = 2100$ MeV at the three measured angles. From top to bottom: $\theta = 0.7°$, 3°, and 9° lab.

much smaller than that attainable by the experimental resolution. These widths are narrow since no strong interaction disintegrations can occur at these masses. More generally, for all structures, due to the large background, the widths and therefore their production cross-sections, are inextricable.

When all three structures at $M = 1004$ MeV, 1044 MeV, and 1094 MeV are observed at most angles and energies, narrow structures are also observed at higher masses, but lightly excited and therefore more rare. Consequently they may be observed with a small SD hence making them less certain. They are kept when observed several times at neighbouring mass values. These results are presented in the following subsections. The final mass is the mean value of the masses observed when the structures were present. The results will be presented later in sect. 7.1, regrouping the different spectra, from different reactions, for each narrow-structure mass.

6.3 The invariant masses from the $pp \rightarrow p\pi^+X$ reaction

Only the results from the $M_{p\pi^+}$ invariant masses will be discussed. The $M_{X\pi^+}$ invariant masses are larger than $M = 1.46$ GeV and the corresponding results will be presented in a forthcoming paper. The maximum mass range of the $M_{p\pi^+}$ varies with the incident proton energy (and is slightly dependent on the spectrometer angle) as indicated in fig. 19. This upper limit is imprecise since the count rates at the upper edge of the $M_{p\pi^+}$ invariant mass are very low. Again, in this mass range several narrow structures were observed although less excited than in $M_X \leq 1.1$ GeV. They were subsequently observed in certain kinematical configurations and sometimes with a low

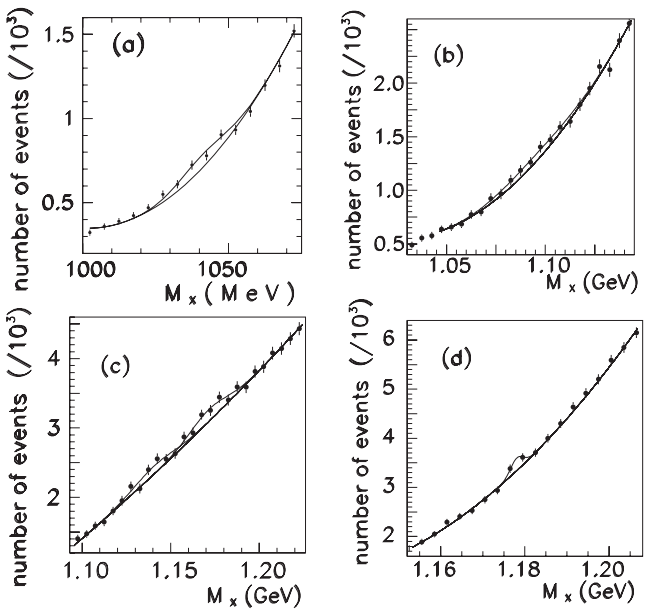

Fig. 31. Number of events in the missing-mass spectra from the $\vec{\mathrm{d}}\mathrm{p} \rightarrow \mathrm{ppX}$ reaction. The experimental conditions corresponding to the inserts (a), (b), (c), and (d) are specified in table 1.

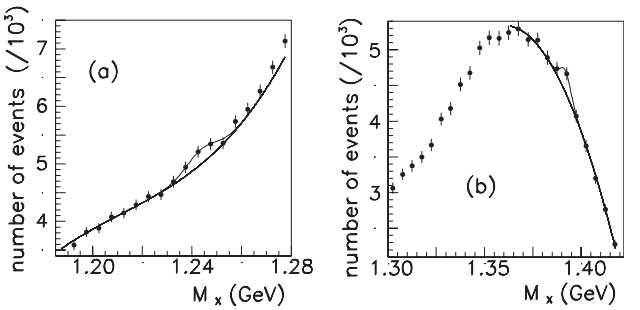

Fig. 32. The $\vec{\mathrm{d}}\mathrm{p} \rightarrow \mathrm{ppX}$ reaction at $T_\mathrm{d} = 2.1$ GeV and $\theta = 17°$. The experimental conditions corresponding to the inserts (a) and (b) are specified in table 2.

SD and so are less certain. These results will be discussed later (see later figs. 41, 42 and 43).

6.4 The missing mass from the $\vec{\mathrm{d}}\mathrm{p} \rightarrow \mathrm{ppX}$ reaction

This reaction was studied some time ago [15]. First results on the tensor analyzing powers and vector analyzing powers of the invariant M_pp mass were studied with the aim of searching for narrow dibaryons. Small structures in the missing mass M_X were observed, but their low SD prevented us from concluding that narrow baryons were observed. The situation is different today since the masses of the narrow structures once observed, are very close to those observed now in the more recent $\mathrm{pp} \rightarrow \mathrm{p}\pi^+\mathrm{X}$ measurements. The results from the $\vec{\mathrm{d}}\mathrm{p} \rightarrow \mathrm{ppX}$ reaction are consistent with the observed structures.

These results are shown in figs. 31, 32, 33, 34, 35, 36, and 37. They will be discussed in the next subsections.

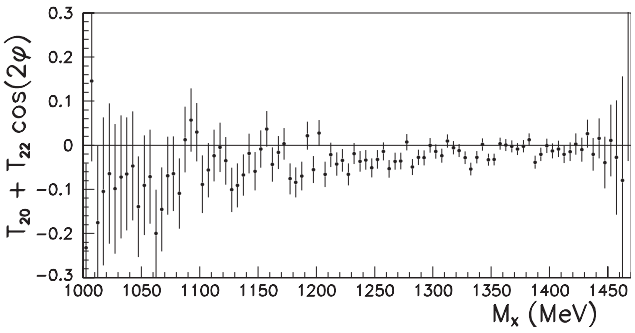

Fig. 33. Tensor analyzing power of the missing mass of the $\vec{\mathrm{d}}\mathrm{p} \rightarrow \mathrm{ppX}$ reaction at $T_\mathrm{d} = 2.1$ GeV and $\theta = 17°$.

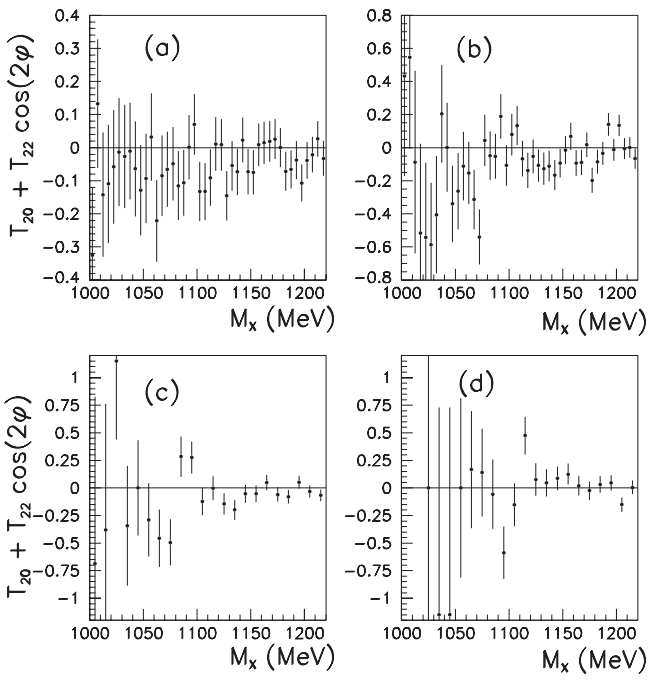

Fig. 34. Tensor analyzing power of the $\vec{\mathrm{d}}\mathrm{p} \rightarrow \mathrm{ppX}$ reaction at $T_\mathrm{d} = 2.1$ GeV and $\theta = 17°$. The four inserts (a), (b), (c), and (d) correspond, respectively, to the following cuts applied on M_pp: $1876 \leq M_\mathrm{pp} \leq 1880$ MeV ($^1S_0$) pp state, $1880 \leq M_\mathrm{pp} \leq 1883$ MeV, $1883 \leq M_\mathrm{pp} \leq 1886$ MeV, and $1886 \leq M_\mathrm{pp} \leq 1889$ MeV.

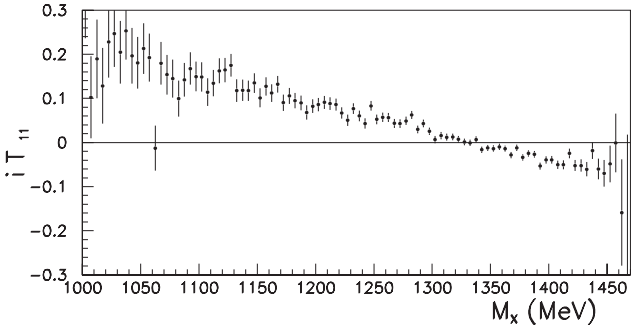

Fig. 35. Vector analyzing power of the $\vec{\mathrm{d}}\mathrm{p} \rightarrow \mathrm{ppX}$ reaction at $T_\mathrm{d} = 2.1$ GeV and $\theta = 17°$.

Table 1. A selection of five missing-mass cross-sections from the $\vec{d}p \rightarrow ppX$ reaction, showing narrow structures. The columns describe each insert, the mass found, the experimental width, the number of standard deviations of the structure, the incident energy, the spectrometer angle, and the cuts performed in the software analysis.

Figure 31	Mass (MeV)	Width (MeV)	SD	T_d (GeV)	θ	Cuts on M_{pp} (MeV)
(a)	1041	8.0	3.05	2.1	17°	$1876 \leq M_{pp} \leq 1889$
(b)	1094.7	17.4	3.0	2.1	17°	$1876 \leq M_{pp} \leq 1880$
(c)	1140.3	11.5	3.0	2.1	17°	$1876 \leq M_{pp} \leq 1880$
(c)	1171.2	10.3	3.95	2.1	17°	$1876 \leq M_{pp} \leq 1880$
(d)	1178.1	1.5	1.85	1.722	0°	no cuts on M_{pp}

Table 2. A selection of two missing-mass cross-sections from the $\vec{d}p \rightarrow ppX$ reaction, showing narrow structures. The columns describe each insert, the mass found, the experimental width, the number of standard deviations of this structure, the incident energy, the spectrometer angle, and the cuts performed with the software.

Figure 32	Mass (MeV)	Width (MeV)	SD	T_d (GeV)	θ	Cuts on M_{pp} (MeV)
(a)	1243.8	6.0	3.2	2.1	17°	$1876 \leq M_{pp} \leq 1880$
(b)	1391.9	2.8	2.6	2.1	17°	$1876 \leq M_{pp} \leq 1880$

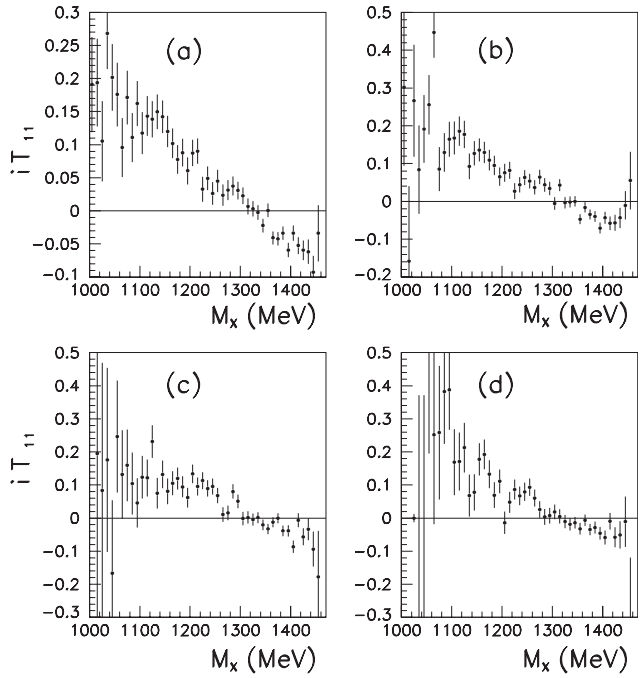

Fig. 36. Vector analyzing power of the $\vec{d}p \rightarrow ppX$ reaction at $T_d = 2.1$ GeV and $\theta = 17°$. The inserts have the same definition as those in fig. 34.

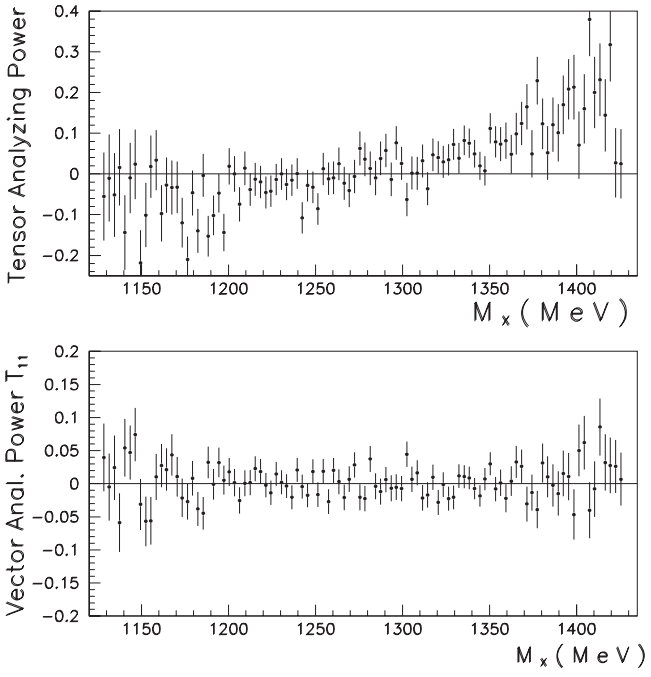

Fig. 37. Tensor and vector analyzing powers of the missing mass of the $\vec{d}p \rightarrow ppX$ reaction at $T_d = 1.722$ GeV and $\theta = 0°$.

Figures 31 and 32 display the number of events (as opposed to cross-sections), since initially corrections for inefficiencies and acceptances were not available. The migration to more modern computing systems has prevented further analysis of this data since there is no further access to equipment required to read the data from the original magnetic tapes. The lack of any sharp variation in the acceptance corrections, as now observed in the $pp \rightarrow p\pi^+X$ data analysis, allows us to consider these spectra.

6.5 Invariant-mass distributions of the $\gamma n \rightarrow p\pi^-\pi^0$ reaction

Different reactions of double-pion photoproduction on a nucleon were studied experimentally and analyzed theoretically [16]. The multitude of baryonic resonances which must be considered in the intermediate states produce different channels which can interfere, and consequently an oscillatory cross-section shape can be observed. However, these oscillations are broad [16] in comparison with the widths considered in the present work and cannot be the

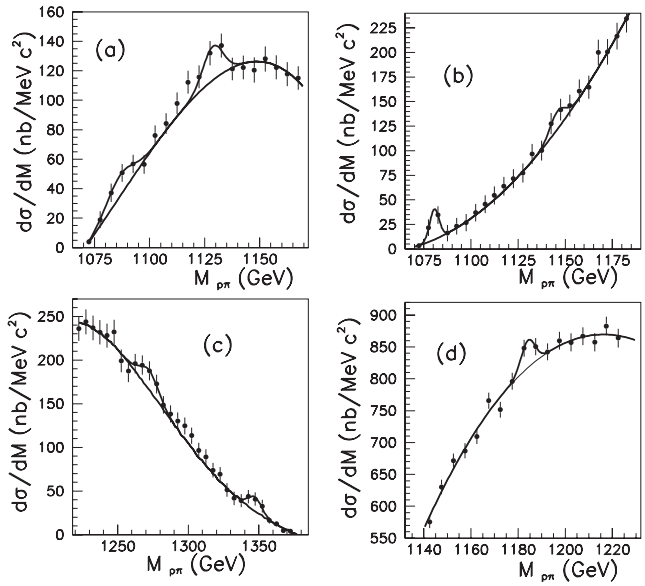

Fig. 38. Invariant-mass distributions of the $\gamma n \rightarrow p\pi^-\pi^0$ reaction [19] showing a selection of cross-sections where small narrow structures were extracted. The experimental conditions corresponding to the inserts (a), (b), (c), and (d) are specified in table 3.

Table 3. The $\gamma n \rightarrow p\pi^-\pi^0$ reaction studied at MAMI [19] (see sect. 6.5). Cross-sections of the invariant $p\pi^0$+$p\pi^-$ mass. A selection of cross-sections where small narrow structures were extracted are presented and related to the four inserts (a), (b), (c), and (d) of fig. 38.

Figure 38	Mass (MeV)	Width (MeV)	SD	Energy range (GeV)
(a)	1086.5	6	3.1	$500 \leq T_\gamma \leq 600$
(a)	1128.8	4.5	3.	$500 \leq T_\gamma \leq 600$
(b)	1080.6	2.5	2.5	$700 \leq T_\gamma \leq 750$
(b)	1145.9	4.0	1.6	$700 \leq T_\gamma \leq 750$
(c)	1272.3	6.6	2.9	$700 \leq T_\gamma \leq 750$
(c)	1347.2	4.7	1.9	$700 \leq T_\gamma \leq 750$
(d)	1184	2.7	2.9	$500 \leq T_\gamma \leq 800$

cause of structures having $\sigma \approx 10$ MeV. The data from such measurements, performed in order to study the reaction mechanism in double-pion photoproduction, cannot generally be used for the present study because of the large spacing between adjacent Nπ invariant masses. This is the case for the total cross-sections of the following reactions: $\gamma p \rightarrow p\pi^-\pi^+$, $\gamma p \rightarrow n\pi^+\pi^0$, and $\gamma p \rightarrow p\pi^0\pi^0$ measured at MAMI [17]. This is also the case for the Compton scattering off the proton [18] measured at MAMI.

An exception to this is the $\gamma n \rightarrow p\pi^-\pi^0$ reaction. This reaction was studied at MAMI [19] in the photon energy range $500 \leq T_\gamma \leq 800$ MeV. The ($p\pi^0$ + $p\pi^-$) spectra were integrated over 50 MeV bins of the incident photon energy. The experiment was clearly not performed with the intention of looking for narrow baryons, and therefore the statistics for this purpose are poor. However, some structures can be observed which were not discussed by

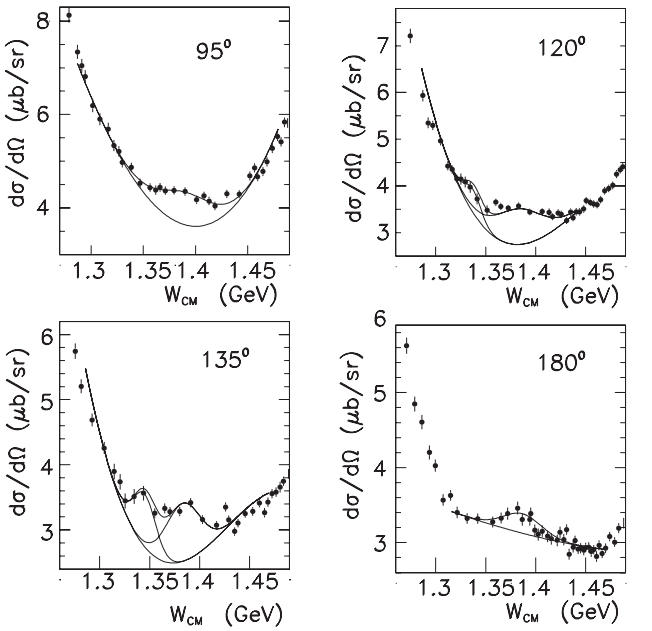

Fig. 39. Excitation functions of $\gamma p \rightarrow \pi^+ n$ cross-sections measured at Bonn [20], after a two-channel integration. The experimental conditions corresponding to the inserts (a), (b), (c), and (d) are described in table 4.

Table 4. Excitation function of the $\gamma p \rightarrow \pi^+ n$ reaction studied at the Bonn electron synchrotron [20].

θ (degrees)	Mass (MeV)	Width (MeV)	SD
95	1390.3	25.4	12.4
120	1336.9	8.7	6.5
120	1383.1	24.3	15.3
135	1345.0	11.3	7.7
135	1383.2	17.5	12.2
180	1386.6	19.1	4.7

the authors. With the aim of observing where they lie with respect to the other narrow structures, we extracted these peak values. Figure 38 shows a selection of the results of [19], and table 3 describes the range of integration of the incident photon energy, the mass extracted and the corresponding SD. Each peak will be discussed separately in this text in sects. 6.9 to 6.10.

6.6 Cross-section of the $\gamma p \rightarrow \pi^+ n$ reaction.

This reaction was studied at the Bonn 2.5 GeV electron synchrotron, using a photon incident energy of $0.3 \leq T_\gamma \leq 2.1$ GeV [20]. The experiment was performed in order to study the electromagnetic structure of the nucleon resonances formed in the *s*-channel. The excitation functions were measured at six different backward angles. At all angles the cross-sections decrease quickly down to a total energy of $W = 1.3$ GeV, and some narrow structures can be observed at larger masses. The cross-sections were integrated over two channels, and fits of these narrow structures in the range $1.3 \leq W \leq 1.44$ GeV were performed.

Figure 39 shows some of the results obtained and correspond to four angles, whereas table 4 describes the quantitative values extracted from the previous fits. As for the previous reaction, the result for each peak will be discussed separately in sects. 6.9 to 6.10.

6.7 The pd → ppX reaction

This reaction was studied with the 305 MeV proton beam of the Moscow Linear Accelerator [21]. The authors observed narrow dibaryons in the pX system and narrow baryonic peaks at 966 MeV, 986 MeV, and 1003 MeV in the missing mass M_{X}. They suggest that the narrow baryons observed at masses below the pion disintegration threshold mass, "are not excited states of the nucleon, but resonance-like states caused by possible existence and decay of narrow dibaryons. They cannot give contribution to the Compton scattering on the nucleon". Their largest mass, 1003 MeV, corresponds to our lightest narrow exotic structure at $M = 1004$ MeV. Their two lightest masses correspond to a range not studied in the present work.

6.8 Structure at M = 1004 MeV

A structure at this mass can be perceived with variable excitation over the background, in the missing mass of the pp → pπ^+X reaction at the three energies (figs. 24, 25, 29, and 30). This low mass is outside the range of the invariant $M_{\mathrm{p}\pi^+}$ mass of the pp → pπ^+X and also outside the range of the missing mass of the $\vec{\mathrm{d}}$p → ppX reaction at $T_{\mathrm{d}} = 1722$ and 2100 MeV.

Two shoulders were observed in the missing mass M_{n} of the p(d)p → π^+pn reaction (deuteron vertex) in an experiment performed at Dubna using 3.34 GeV/c deuterons [22]. The masses of these shoulders: $M \approx 1.0$ GeV and $M \approx 1.05$ GeV are close to the masses of our two first narrow baryons. A peak at the same mass was observed in the pd → ppX reaction [21] (see previous sect. 6.7).

6.9 Structure at M = 1044 MeV

A small structure at this mass was observed in the missing mass of the pp → pπ^+X reaction at all three incident energies studied (figs. 24, 25, 29, and 30). This low mass is also outside the range of the invariant $M_{\mathrm{p}\pi^+}$ mass of the pp → pπ^+X. There is an indication (with a small SD) of the presence of a structure in the missing mass M_{X} of the $\vec{\mathrm{d}}$p → ppX reaction. Weak discontinuities can be seen in insert (a) of fig. 31, in the tensor analyzing power (fig. 34) and in the vector analyzing power (fig. 36).

A shoulder at this mass was also observed in the missing mass M_{n} of the previously cited Dubna experiment, namely the p(d)p → π^+pn reaction [22].

6.10 Structure at M = 1094 MeV

A structure at this mass is clearly observed in the missing mass of the pp → pπ^+X reaction (figs. 24, 25, 29, and 30). As an example, let us consider some quantitative information concerning this missing-mass peak. At $T_{\mathrm{p}} = 1.805$ GeV and $\theta = 9°$, we have $M_{\mathrm{X}} = 1092.3$, $\sigma = 10.7$ MeV, and SD = 8.1. This low mass is also outside the useful range of the invariant $M_{\mathrm{p}\pi^+}$ mass of the pp → pπ^+X since it is too close to threshold. There are some small indications of the presence of a different narrow excitation, around this mass, in several analyzing powers of the $\vec{\mathrm{d}}$p → ppX reaction. They appear in fig. 33 and in inserts (c) and (d) of fig. 34.

Using the cross-sections of the γn → $\pi^-\pi^0$p reaction studied at MAMI [19], two structures were extracted in the mass region close to 1085 MeV. These results are shown in fig. 38 and table 3. The invariant pπ masses found 1086.5 MeV and 1080.6 MeV, are too small and imprecise since they are close to threshold ($\approx$ 1075.5 MeV). The γp → $\pi^+\pi^0$n reaction was also studied at MAMI [23]. Although the authors said that "deviations of the experimental data from the phase space distribution are evidence for resonant or meson intermediate states in the π^+ π^0 production", it is useful to point out that in $M_{\mathrm{n}\pi^0}$ and $M_{\mathrm{n}\pi^+}$ invariant masses, a narrow peak at $M \approx 1.095$ GeV is observed at low incident photon energies (their fig. 2). The virtual Compton scattering in the nucleon resonance region was studied at JLAB (Hall A) [24]. A small peak ($\sigma \approx 12$ MeV) was observed (insert (a) of their fig. 3) at $W \approx 1.098$ GeV.

6.11 Structure at M = 1136 MeV

This was observed in the $M_{\mathrm{p}\pi^+}$ invariant mass at $T_{\mathrm{p}} =$ 1805 MeV and 2100 MeV (see table 5). Figure 40 shows four inserts where a small peak was extracted from the data in this mass region. Table 5 indicates the masses found, the corresponding experimental widths, the number of SD, the incident energy, and the spectrometer angle.

A small structure at $M_{\mathrm{X}} = 1140$ MeV was observed in the $\vec{\mathrm{d}}$p → ppX reaction (insert (c) of fig. 31). Small structures in this mass region were extracted at $M \approx 1129$ MeV and 1146 MeV, from the γn → p$\pi^-\pi^0$ reaction (inserts (a) and (b) of fig. 38, and table 3).

6.12 Structure at M = 1173 MeV

Figure 41 shows four inserts showing a shoulder at this mass in the invariant $M_{\mathrm{p}\pi^+}$ spectrum. Table 6 describes the corresponding results. This structure is not observed in the missing mass. Only at $T_{\mathrm{p}} = 1805$ MeV and $\theta = 3.7°$ is there a very small peak at 1162 MeV, but with a very low SD (SD = 1).

A small structure at $M_{\mathrm{X}} = 1178$ MeV was observed in the $\vec{\mathrm{d}}$p → ppX reaction at $T_{\mathrm{d}} = 1722$ MeV (insert (d) of fig. 31). In the same reaction at $T_{\mathrm{d}} = 2100$ MeV, a structure was extracted at 1171 MeV (insert (c) of fig. 31).

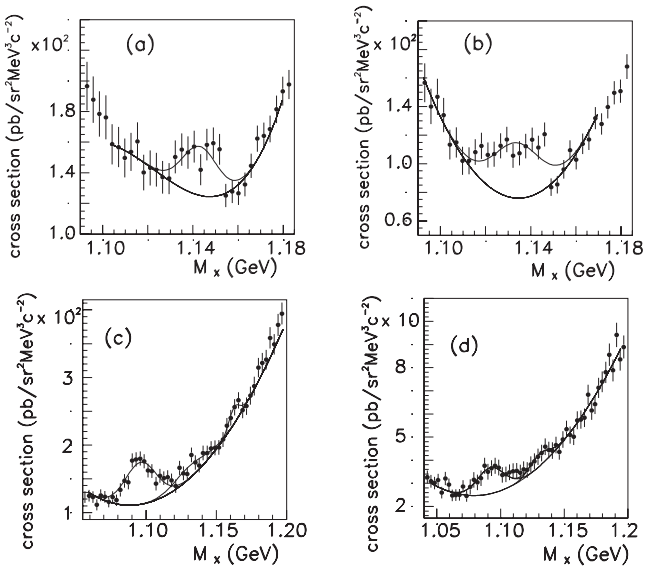

Fig. 40. A selection of cross-sections where a narrow structure at $M_{\rm X} = 1136$ MeV was observed. The experimental conditions corresponding to the inserts (a), (b), (c), and (d) are described in table 5.

Table 5. Cross-sections of the invariant $M_{\rm p\pi^+}$ mass from the $\rm pp \rightarrow p\pi^+X$ reaction. The extracted values are given and are related to the four inserts of fig. 40, justifying the extraction of a narrow structure at $M = 1136$ MeV.

Figure 40	Mass (MeV)	Width (MeV)	SD	$T_{\rm p}$ (GeV)	θ
(a)	1143	7.9	6.3	2.1	0.7°
(b)	1133.7	10.6	11	2.1	3°
(c)	1130.4	11.3	4.9	1.805	3.7°
(d)	1130.8	8.6	3.6	1.805	9°

A small peak was observed at 1184 MeV (insert (d) of fig. 38), in the $\gamma \rm p \rightarrow p\pi^+\pi^-$ reaction studied at MAMI [19].

There is an indication of a small and narrow structure at $W \approx 1168$ MeV, in the total π^0 electro-production cross-section studied at JLAB (Hall A) [24] (see $\sigma_{\rm Tot}$ in their fig. 1). In the same paper there is also a small indication at the same mass observed in the virtual Compton scattering excitation curve (at $\Phi = 0°$).

6.13 Structure at M = 1249 MeV

Figure 42 is comprised of four inserts showing a shoulder in the invariant $M_{\rm p\pi^+}$ mass from the $\rm pp \rightarrow p\pi^+X$ reaction at $T_{\rm p} = 1.52$ GeV. Table 7 describes these results.

A shoulder was also observed in the missing mass of the $\vec{\rm d}\rm p \rightarrow ppX$ reaction (insert (a) of fig. 32 and table 2).

There is a very small indication of a structure at a mass close to 1246 MeV in the total π^0 electro-production cross-section studied at JLAB (Hall A) [24].

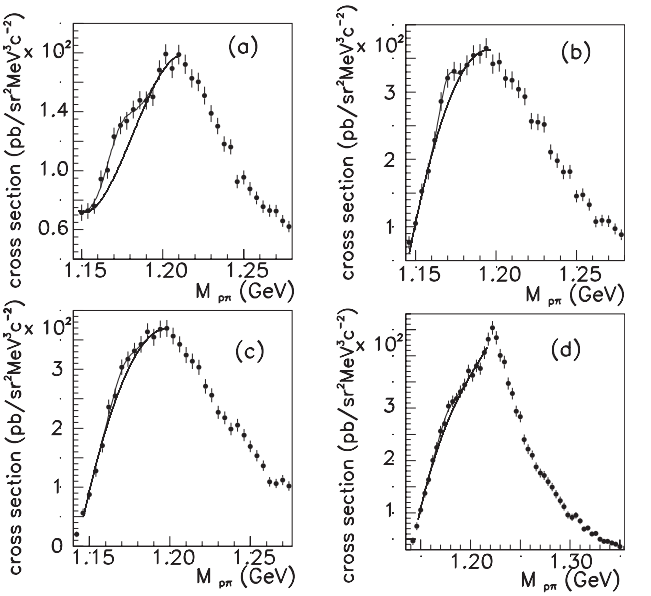

Fig. 41. A selection of cross-sections where a narrow structure at $M_{\rm X} = 1173$ MeV was observed. The experimental conditions corresponding to the inserts (a), (b), (c), and (d) are described in table 6.

Table 6. Cross-sections of the invariant $M_{\rm p\pi^+}$ mass from the $\rm pp \rightarrow p\pi^+X$ reaction. The extracted values are given and are related to the four inserts of fig. 41 justifying the extraction of a narrow structure at $M = 1173$ MeV.

Figure 41	Mass (MeV)	Width (MeV)	SD	$T_{\rm p}$ (GeV)	θ
(a)	1173.4	8.1	7	1.52	13°
(b)	1166.9	4.2	3.4	1.52	0°
(c)	1170.4	5.9	2.8	1.52	2°
(d)	1176.6	7.8	3.1	1.805	6.7°

6.14 Structure at M = 1277 MeV

Figure 43 shows three inserts where a shoulder in the invariant $M_{\rm p\pi^+}$ mass and in the missing mass of the $\rm pp \rightarrow p\pi^+X$ reaction is observed. Table 8 regroups these results.

A shoulder was extracted at 1272 MeV in the $\gamma \rm n \rightarrow p\pi^0\pi^-$ reaction studied at MAMI [19]. Figure 38 (insert (c)) and table 3 show the associated values.

6.15 Structure at M = 1339 MeV

A small structure in the missing mass $M_{\rm X} = 1327.1$ MeV was observed at $T_{\rm p} = 2.1$ GeV and $\theta = 9°$ (fig. 43 (d)). This mass should normally not be mentioned from this single result, but peaks at nearby masses were observed in previously published data from other experiments. Two structures were extracted from the $\gamma \rm p \rightarrow \pi^+ n$ cross-section [20] at $M = 1337$ MeV for $\theta = 120°$ and at 1345 MeV for $\theta = 135°$ (see fig. 39). A peak was extracted from the $\gamma \rm n \rightarrow p\pi^0\pi^-$ reaction [19] at $M = 1347$ MeV (see fig. 38).

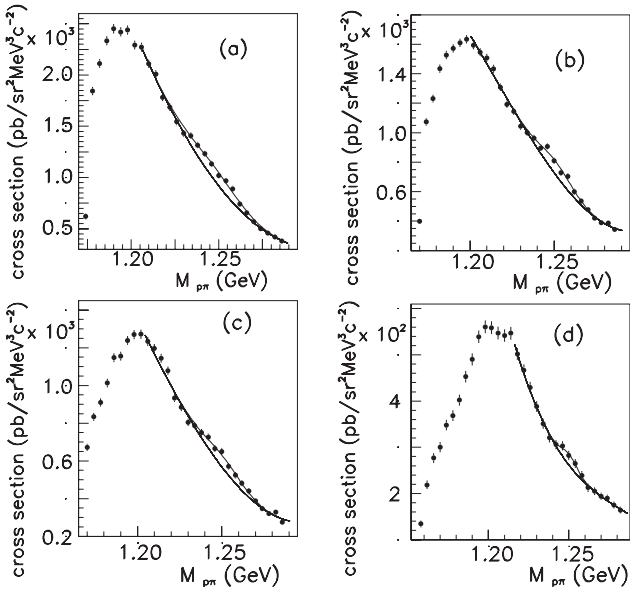

Fig. 42. A selection of cross-sections where a narrow structure at $M_X = 1249$ MeV was observed. The experimental conditions corresponding to the inserts (a), (b), (c), and (d) are described in table 7.

Table 7. Cross-sections of the invariant $M_{p\pi^+}$ mass from the $pp \to p\pi^+X$ reaction. The extracted values are given and are related to the four inserts of fig. 42 justifying the extraction of a narrow structure at $M = 1249$ MeV.

Figure 42	Mass (MeV)	Width (MeV)	SD	T_p (GeV)	θ
(a)	1247.3	13.9	10.4	1.52	0°
(b)	1251.1	9.5	8.3	1.52	2°
(c)	1250.7	10.8	7.3	1.52	5°
(d)	1250.2	5.0	3.0	1.52	9°

6.16 Structure at M = 1384 MeV

Figure 44 shows two inserts where a shoulder in the missing mass of the $pp \to p\pi^+X$ and $dp \to ppX$ reactions is observed. Table 9 describes the results. A structure at $M = 1369$ MeV, $\sigma = 14.5$ MeV, and SD = 3.6 was already observed in fig. 43 (d).

A peak at the same mass was extracted from the cross-sections of the $\gamma p \to \pi^+ n$ reaction studied at Bonn [20]. It was observed at four angles. Table 4 and fig. 39 show the results extracted after an integration over two channels. The mean mass value from that experiment is $M = 1385.8$ MeV, very close to the mass 1384 MeV extracted from our data.

7 Discussion

7.1 General discussion

Three strongly excited structures were observed in the missing-mass spectra at $M_X = 1004$ MeV, 1044 MeV,

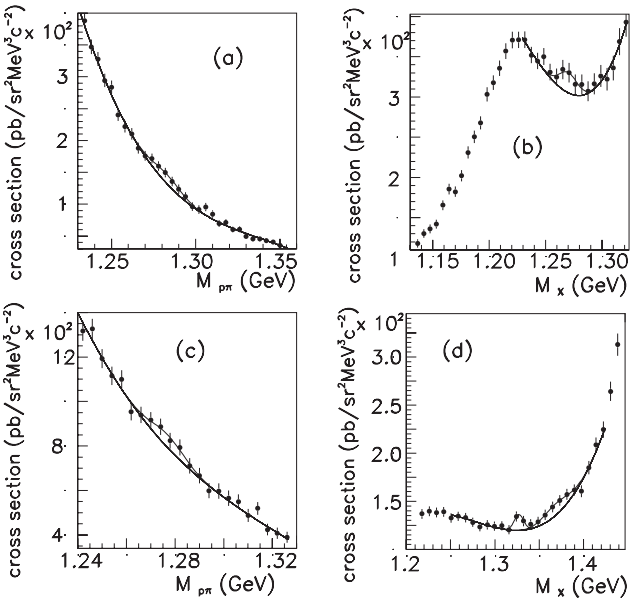

Fig. 43. A selection of cross-sections where a narrow structure at $M_X = 1277$ MeV was observed. The experimental conditions corresponding to the inserts (a), (b), and (c), are described in table 8.

Table 8. Cross-sections of the invariant $M_{p\pi^+}$ mass and of the missing mass M_X from the $pp \to p\pi^+X$ reaction. The extracted values are given and are related to the three inserts (a), (b), (c) of fig. 43 justifying the extraction of a narrow structure at $M = 1277$ MeV. Insert (d) illustrates the observation of a structure close to $M = 1330$ MeV.

Figure 43	Mass (MeV)	Width (MeV)	SD	T_p (GeV)	θ	Observable
(a)	1282.8	8.3	3.5	1.805	6.7°	$M_{p\pi^+}$
(b)	1270.0	8.1	3.2	1.805	3.7°	M_X
(c)	1277.0	6.6	2.4	2.1	9°	$M_{p\pi^+}$
(d)	1327.1	5.3	2.7	2.1	9°	M_X

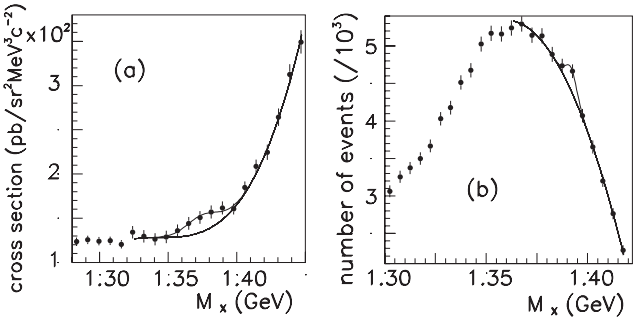

Fig. 44. A selection of cross-sections where a narrow structure at $M_X = 1384$ MeV was observed. The experimental conditions corresponding to the inserts (a) $pp \to p\pi^+X$ reaction and (b) $dp \to ppX$ reaction are described in table 9.

Table 9. Cross-sections of the missing mass M_X from the $pp \rightarrow p\pi^+X$ and $dp \rightarrow ppX$ reactions. The extracted values are given and are related to the two inserts of fig. 44 justifying the possibility of the extraction of a narrow structure close to $M = 1384$ MeV.

Figure 44	Mass (MeV)	Reaction	Width (MeV)	SD	T (GeV)	θ
(a)	1375.3	$pp \rightarrow p\pi^+X$	12.1	3.7	1.805	6.7°
(b)	1391.9	$dp \rightarrow ppX$	2.8	2.6	2.1	17°

Table 10. Experiments whose results are displayed in fig. 45. The last column (j) of fig. 45 shows also one mass ($M = 1136$ MeV) extracted from the $np \rightarrow pX$ experiment from LAMPF [13].

Column	Reaction	Variable	Incident energy (MeV)	Reference
(a)	$pp \rightarrow \pi^+pX$	M_X	1520	this work
(b)	$pp \rightarrow \pi^+pX$	M_X	1805	this work
(c)	$pp \rightarrow \pi^+pX$	M_X	2100	this work
(d)	$pp \rightarrow \pi^+pX$	$M_{p\pi}$	1520	this work
(e)	$pp \rightarrow \pi^+pX$	$M_{p\pi}$	1805	this work
(f)	$pp \rightarrow \pi^+pX$	$M_{p\pi}$	2100	this work
(g)	$dp \rightarrow ppX$	M_X	1722	this work
(h)	$dp \rightarrow ppX$	M_X	2100	this work
(i)	$\gamma n \rightarrow p\pi^-\pi^0$	$M_{p\pi}$	500–800	[19] (MAMI)
(j)	$\gamma p \rightarrow \pi^+n$	W_{CM}	300–2000	[20] (Bonn)

and 1094 MeV. Several lightly excited structures were observed at heavier masses. They were considered when observed several times at the same mass to within a few MeV. Their non-observation in other spectra might be associated with their small cross-section, making them difficult to extract or observe. The existence of these structures is strengthened by the fact that they are usually observed in invariant masses. Indeed the confidence in small peaks observed in missing masses may be smaller. Moreover, these structures are observed in various independent experiments. Some peaks were not considered since they were not observed several times in our data. An example of such a case is the spectrum of the $M_{p\pi}$ invariant mass at $T_p = 1.805$ GeV and $\theta = 0.75°$, where a structure was extracted at 1232 MeV.

Figure 45 shows all the masses discussed previously along with those presented from our measurements and those extracted from previously published data from various experiments. The horizontal bands correspond to the mean mass ±3 MeV. Table 10 allows to connect the different experiments to the marker plot in fig. 45. It is worth noting that very few mass structures lie outside the range defined by the horizontal bands of fig. 45.

The only high-precision experiment previously dedicated to looking for narrow baryons was performed at TRIUMF [25]. The reaction studied was $pp \rightarrow B^{++}n$ (in fact $p + CH_2 \rightarrow B^{++}X$) at 460 MeV. In this experiment a hypothetical doubly charged baryon B^{++} was looked for behind a spectrometer and was not observed in the limit of 0.75 pb/sr. There were two reasons to look for a doubly charged baryon:

– if it exists, it would be easier to identify among a large flux of singly charged protons and pions,

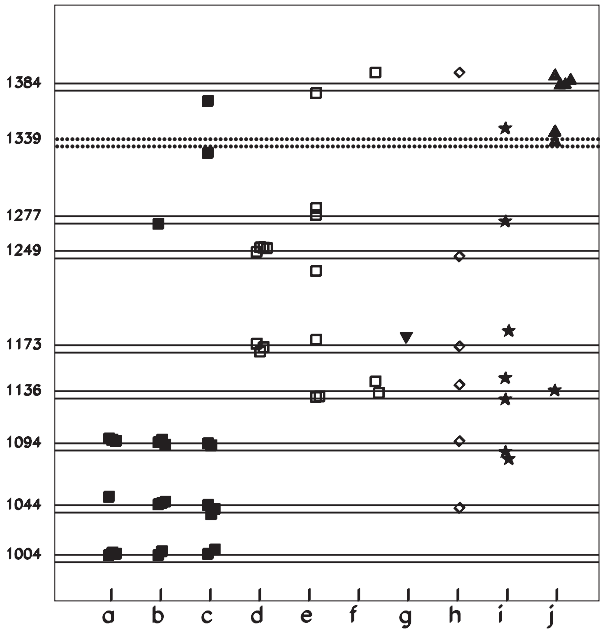

Fig. 45. Narrow-structure baryonic masses observed in cross-sections from different reactions. These reactions are described in table 10.

– since only a weak decay would be possible ($B^{++} \rightarrow pe^+\nu_e$) its lifetime should be long enough, at least 10^{-2} s on the basis of the hyperon lifetime, making it possible to detect behind a spectrometer [25]. This hypothetical doubly charged baryon, with isospin $T = 3/2$, was not observed. This supports our tentative isospin $T = 1/2$ attribution for possible first exotic baryons. Such an isospin attribution agrees with our quark cluster mass

formula (see later, sect. 7.2) and with the diquark model of Konno [26] (see later, sect. 7.3).

Another experiment was studied earlier at KEK [27], using a 12 GeV proton beam, with the aim of looking for long-lived exotic hadrons with charge ± 2 or $-5/3$. Once again no candidate was found. This experiment was performed in somewhat unfavorable experimental conditions: composite target (platinium), very long detection line (36 m), small solid angle ($\Delta\Omega \approx 1$ msr), and a small momentum acceptance ($\Delta p/p \approx \pm 3\%$). The negative result again agrees with the tentative isospin attribution ($T = 1/2$) of our narrow, low-mass exotic baryons. Below $M = 1.2$ GeV, only one calculated mass (at 1139 MeV) can have $T = 1/2$ or $3/2$ (see next subsection).

Figure 19 shows the masses of the narrow structures observed in this work. We note that in most cases a structure was observed when it could be observed.

Since we have not observed the structures in excitation spectra with slowly increasing incident energy, we are sheltered from any possible cusp effect (threshold energy for the production of any heavier meson). Moreover the threshold energy for these cusp effects would be different for different reactions, such as pp $\rightarrow$ pπ^+X and dp $\rightarrow$ ppX. This effect is the only physical process sometimes advocated to explain the experimentally observed narrow structures.

As already discussed, there is no room for new, low-mass and narrow baryons within the many-quark models [10]. These models use several parameters, and the baryonic masses calculated depend on the set of parameters chosen (see for example [28]). Within the mass range discussed in this work, the number of baryons found is equal to the number of experimental baryons for each T and J^P even if the calculated masses are sometimes much lower. For example, in the calculation of [28], the lowest N $1/2^-$ and N $3/2^-$ states are found at masses close to 1360 MeV when their first set of parameters is used.

The experimental determination of the quantum numbers of the observed exotic baryons is outside the scope of the present work. This requires the knowledge of the angular distributions. Also knowing the parity would be very useful, since it would allow the verification of the assumption concerning the number of quarks (antiquarks) involved.

7.2 Quark cluster mass formula

An interpretation was tentatively proposed to explain the observed narrow and exotic hadrons, associating them with two colored-quark clusters. In our previous papers, dedicated to narrow dibaryon [1] and meson [5] searches, it was shown that the masses of the experimentally observed narrow structures were in good agreement with those obtained through a simple phenomenological mass formula using two-cluster $q^n\bar{q}^m$-$q^p\bar{q}^r$ configurations. It was shown in the already quoted references that such an attempt allows to reproduce the masses with models using a very small number of adjusted parameters (from zero to two), depending on the hadronic species in question. In these models, where the exotic hadron arises from a partial deconfinement, we would expect small narrow amplitude signatures throughout the complete hadronic spectra. This paper presents the analysis and the results obtained in order to check this idea in low-mass baryons. The following mass formula is used:

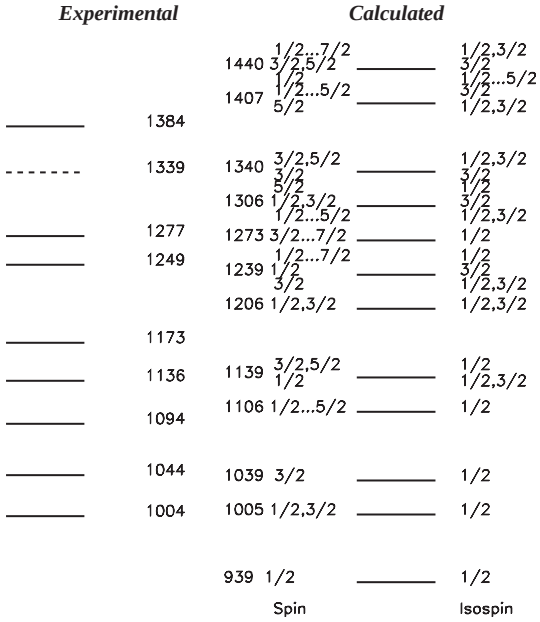

Fig. 46. Narrow baryonic experimental and calculated masses. Equation (2) was used (see text for more details).

$$M = M_0 + M_1[i_1(i_1+1) + i_2(i_2+1) + (1/3)s_1(s_1+1) + (1/3)s_2(s_2+1)], \quad (2)$$

where $s_1(s_2)$ and $i_1(i_2)$ are the first (second) cluster spin and isospin values. This formula was derived some years ago [29] for two clusters of quarks at the ends of a stretched bag in terms of color magnetic interactions.

The same approach is employed here. Equation (1) involves a large degeneracy. We made the assumption that the simplest configuration is preferred, otherwise the possible spin and isospin will increase and the parity will be degenerate since additional $q\bar{q}$ configurations will always be possible. The two parameters, described in [3], were adjusted in order to find the mass, spin, and isospin values of the nucleon and the Roper N*(1440) baryons. Such assumptions lead to the values $M_0 = 838.2$ MeV and $M_1 = 100.3$ MeV. This does not mean that we consider our new exotic baryons to be excited states of the nucleon. There is no simple overlap between q^3 and $q\bar{q}$-q^3, or q^2-q wave functions.

Figure 46 shows the masses, spins, and isospins obtained using eq. (1). We observe the surprisingly good agreement between the experimental masses and the masses calculated without any adjustable parameters, for the four first states. The agreement is in fact rather good for all masses, except two states at $M = 1173$ MeV and $M = 1384$ MeV. The absence of several masses, predicted by the previous formula, might be related to the fact that

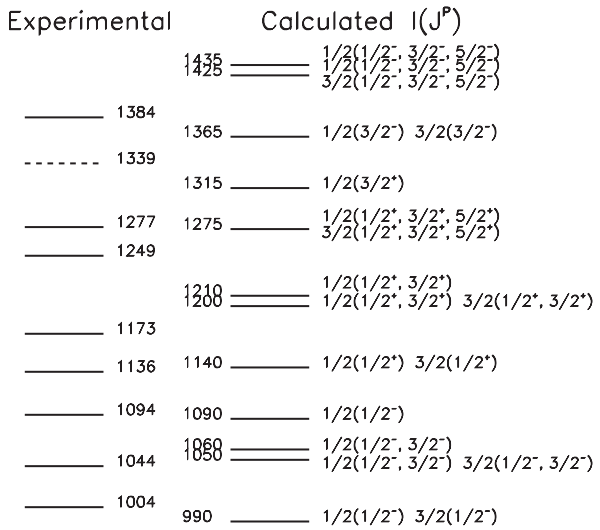

Fig. 47. Narrow baryonic experimental and calculated masses. The calculation corresponds to the diquark cluster model [26].

they are weakly excited. It is not excluded that more precise experiments will, in the future, observe these states. Below the pion emission threshold at 1075 MeV, the only possible decay channel is the radiative one, and the observed width is due to the experimental resolution.

7.3 The diquark cluster model

The diquark cluster model was developed over many years [26]. It was used to calculate the masses of the narrow mesonic resonances, the masses of narrow dibaryons, the mass of the exotic $I = 2$ meson, and the masses of narrow baryonic states. The model does not assume the existence of colored-quark clusters. Different parameters were used, which were all determined previously using the data of baryon masses and the ETH group πd phase shifts. The model assumes that these baryons consist of a diquark and a quark, and that the residual interaction between them is negligibly weak. Figure 47 shows the masses of the exotic baryons calculated within this model, the isospin and spin of the levels, and the comparison with the experimental masses observed in this work. With the exception of the levels at $M = 1173$ MeV and $M = 1249$ MeV, we see that the masses calculated are close to the masses observed experimentally. Once again, there are levels predicted but not observed, and it is not excluded that they exist and could be measured in dedicated experiments in the future.

7.4 The metastable levels model

It was assumed [30] that the first narrow baryons (with masses lower than 1075 MeV), are metastable levels in the three-quark system, as a member of a total antisymmetric representation of the spin-flavor group (20-plet of the $SU(6)_{FS}$) . Since such states cannot be excited by one photon or decay to γN, the simplest decay channel is assumed to be 2γN. In that case, they will not contribute to the Compton scattering.

7.5 Excitation of collective states of the quark condensate

A model was proposed, which associates the narrow baryonic states below the π threshold production to the multiproduction of a genuine virtual Goldstone boson with a mass close to 20 MeV [31]. This model explains not only the combined experimental results for the narrow nucleon states presented above, but also the states observed in the missing mass M_X of the pd $\rightarrow$ ppX reaction [21] and the rather equidistant level spacing of the narrow dibaryons observed experimentally [1].

7.6 The chiral-scale bag model

This (CSB) model [32] deals with chiral and scale symmetries of QCD and their violations. It predicts small radii color confinement, and found that the ground states of $SU(3)$ hadrons could be treated as predominantly multi bag states ($Bag\overline{Bag}Bag$ for baryons). This picture allows low-mass, narrow excitations with a mean distance $\approx$ 50 MeV between the almost degenerated spin-isospin states that appear in strongly bound systems dealing with Bag and $\overline{Bag}$. These narrow excitations are expected for all stable or narrow $SU(3)$ hadrons.

7.7 The chiral constituent quark model

In the chiral constituent quark model, the calculated spectrum of N-like $qqqq\bar{q}$ states [33] exhibits two states $J^P = 1/2^+$ and $3/2^+$, $(T = 1/2)$ at $M \approx 1366$ MeV. This mass is not very far from our experimentally observed state at 1384 MeV. There is no indication concerning the width of this calculated state. Since there are no lower calculated masses, an identification between this calculated state and the one found experimentally at $M = 1384$ MeV, is rather improbable.

7.8 The meson-baryon loops model

This model is based on the calculation of the contribution of meson-baryon loops to the exotic mass operator [34]. Only one meson (the pion) is introduced in the intermediate state. This simplification is justified when low baryonic masses are studied. When restricting its calculation to isotopic spin and spin equal to 1/2, the author finds six possible exotic baryons with alternate parities below the pion production baryonic mass threshold, namely between 963 and 1079 MeV. In the mass range between 1.0 and 1.08 GeV, the calculation predicts the existence of four exotic baryonic resonances (with $T = 1/2$) at $M = 1010$ MeV ($J^P = 1/2^-$), $M = 1033$ MeV ($J^P = 1/2^+$), $M = 1056$ MeV ($J^P = 1/2^-$), and $M = 1079$ MeV ($J^P = 1/2^+$).

8 Conclusion

Narrow baryonic structures were observed in the missing mass and in the invariant mass of the $pp \to p\pi^+X$ and $\vec{d}p \to ppX$ reactions. If we leave aside the states with masses $1.0 \leq M \leq 1.1$ GeV, the ratio of peak to background is small. However, there is no structure without at least one peak extraction with a number of SD ≥ 3.1 (see tables 1 to 9). Many checks were undertaken which allowed to conclude that these structures are genuine and not produced by experimental artifacts. Their masses and widths were extracted using polynomials for the background and Gaussians for peaks. The widths found are not of a high precision since these peaks are usually much smaller than the physical background. The production cross-sections are therefore not precise, and are not discussed further.

The possibility of associating these peaks with dynamical rescattering among final particles, was eliminated for two reasons:

- the structures are narrow,
- they are not spread but they are observed at stable masses for different scattering angles and different incident energies.

We concluded that these peaks correspond to new baryons. There is no room for such states within the many theoretical constituent quark models. Indeed the chiral constituent quark model is known [35] to yield a spectrum for the qqq states which agrees well with the empirical baryon spectrum up to $M \approx 1700$ MeV. Moreover, there is no reason for calculations, performed within the qqq assumption, to explain the relatively narrow widths observed in our data. A calculation performed within a chiral quark model, investigated the hadronic π and η decay modes of N and Δ resonances [36] and the authors found various decay widths which were dependent on several assumptions. However, for the only baryon that they considered in the mass range of the present study, the Roper resonance N_{1440} $1/2^+$, they calculated a width of the order of several hundreds of MeV for the $\Gamma(N^* \to N\pi)$ decay mode.

Therefore, we tentatively associate our narrow baryons with exotic baryons made of two colored-quark clusters. The experimental masses agree well with the masses calculated within a phenomenological relation derived twenty years ago for two colored clusters in a spherical MIT-type bag. The formula is used as a phenomenological one, but allows to determine the two parameters leading to the masses, spins, and isospin of the nucleon and the Roper resonance. This does not mean that we consider them to be excited states of the nucleon. Indeed, there is no simple overlap between q^3 and $q\bar{q} - q^3$, or $q^2 - q$ wave functions.

Even if the hadronic picture dominated by the baryonic resonances is the relevant degree of freedom, quarks may also be relevant at energies as low as the ones considered in this work, and at low-momenta transfer. Therefore, the belief of well-separated regions, one for the quark-gluon picture and the other for the hadronic picture appears to be too simple.

We thank Dr P. Pedroni who provided us with numerical values of the cross-sections from the $\gamma n \to p\pi^-\pi^0$ reaction studied at MAMI. We thank Prof. H. Fischer for this letter saying that he —and his collaborators— were convinced that the unusual behavior of their differential cross-sections is a real effect.

References

1. B. Tatischeff, J. Yonnet, M. Boivin, M.P. Comets, P. Courtat, R. Gacougnolle, Y. Le Bornec, E. Loireleux, F. Reide, N. Willis, Phys. Rev. C **59**, 992 (1999).
2. Yu.A. Troyan, V.N. Pechenov, E.B. Plekhanov, A.Yu. Troyan, S.G. Arakelian, V.I. Moroz, A.P. Ierusalimov, *Proceedings of the XIII International Seminar on High Energy Physics Problems, Dubna 1998*, edited by A.M. Baldin, V.V. Burav, Vol. **II** (Joint Institute for Nuclear Research, Dubna, 1998) p. 10; Phys. At. Nucl. **63**, 1562 (2000).
3. B. Tatischeff, J. Yonnet, N. Willis, M. Boivin, M.P. Comets, P. Courtat, R. Gacougnolle, Y. Le Bornec, E. Loireleux, F. Reide, Phys. Rev. Lett. **79**, 601 (1997).
4. J. Yonnet, B. Tatischeff, M. Boivin, M.P. Comets, P. Courtat, R. Gacougnolle, Y. Le Bornec, E. Loireleux, F. Reide, N. Willis, Phys. Rev. C **63**, 014001 (2000).
5. B. Tatischeff, J. Yonnet, M.P. Rekalo, M. Boivin, M.P. Comets, P. Courtat, R. Gacougnolle, Y. Le Bornec, E. Loireleux, F. Reide, N. Willis, Phys. Rev. C **62**, 054001 (2000).
6. Yu.A. Troyan, E.B. Plekhanov, V.N. Pechenov, A.Yu. Troyan, A.V. Beljaev, A.P. Jerusalimov, S.G. Arakelian, Part. Nucl. Lett. **6[103]**, 25 (2000); Yu.A. Troyan, E.B. Plekhanov, V.N. Pechenov, A.Yu. Troyan, S.G. Arakelian, A.P. Jerusalimov, JINR Rapid Commun. **5[91]**, 33 (1998); M.A. Ananjeva *et al.* JINR preprint P1-98-378 (in Russian).
7. M. Koll, R. Ricken, D.Merten, B.C. Metsch, H.R. Petry, Eur. Phys. J. A **9**, 73 (2000).
8. CERN Program Library Long Writeup W5013.
9. W. Bertozzi *et al.*, Nucl. Instrum. Methods **141**, 457 (1977).
10. S. Capstick, W. Roberts, Prog. Part. Nucl. Phys. **45**, 0S241 (2000).
11. The structure at $M = 1.044$ GeV is rather weakly excited at $T_p = 1.52$ GeV, $\theta = 2^\circ$.
12. B. Tatischeff, J. Yonnet, *Proceedings of the XIII International Seminar on High Energy Physics Problems, Dubna 1998*, edited by A.M. Baldin, V.V. Burav, Vol. **II** (Joint Institute for Nuclear Research, Dubna, 1998) p. 29.
13. B.E. Bonner, C.L. Hollas, C.R. Newsom, P.J. Riley, G. Glass, M. Jain, B.J. VerWest, Phys. Rev. D **27**, 497 (1983).
14. X. Jiang, R. Gilman, R. Ransome, P. Markowitz, T.-H. Chang, C.-C. Chang, G.A. Peterson, D.W. Higinbotham, M.K. Jones, N. Liyanage, J. Mitchell, Phys. Rev. C **67**, 028201 (2003).
15. B. Tatischeff, M.P. Combes-Comets, P. Courtat, R. Gacougnolle, Y. Le Bornec, E. Loireleux, F. Reide, N. Willis, Phys. Rev. C **45**, 2005 (1992).
16. L.Y. Murphy, J.M. Laget, Internal Report (1996), DAPNIA-SPhN-96-10.
17. A. Braghieri *et al.*, Phys. Lett. B **363**, 46 (1995).
18. S. Wolf *et al.*, Eur. Phys. J. A **12**, 231, (2001).

19. A. Zabrodin *et al.*, Phys. Rev. C **60**, 055201, (1999).
20. H.W. Dannhausen, E.J. Durwen, H.M. Fisher, M. Leneke, W. Niehaus, F. Takasaki, Eur. Phys. J. A **11**, 441 (2001).
21. L.V. Fil'kov, V.L. Kashevarov, E.S. Konobeevski, M.V. Mordovskoy, S.I. Potashev, V.A. Simonov, V.M. Skorkin, S.V. Zuev, nucl-th/0101021; Eur. Phys. J. A **12**, 369 (2001); R. Beck, S.N. Cherepnya, L.V. Fil'kov, V.L. Kashevarov, M. Rost, Th. Walcher, nucl-th/0104070.
22. J. Hlavácova, V.V. Glagolev, A.K.Kacharova, S.A. Kushpil, N.B. Ladygina, R.M. Lebedev, A.G. Mamulashvili, G. Martinská, M.S. Nioradze, B. Pastirčák, T. Siemiarczuk, J. Urbán, K.U. Khairetdnikov, M.S. Khvastunov, Phys. At. Nucl. D **60**, 391 (1997).
23. W. Langgärtner *et al.*, Phys. Rev. Lett. **87**, 052001, (2001).
24. G. Laveissiere *et al.*, *Proceedings of the NSTAR 2001 Workshop on the Physics of Excited Nucleons, Mainz 2001*, edited by D. Drechsel, L. Tiator (World Scientific, Singapore, 2001) p. 271.
25. S. Ram, R. Abegg, D. Ashery, D. Frekers, R. Helmer, R.S. Henderson, K.P. Jackson, C.A. Miller, S. Nussinov, E. Piasetzky, A. Rahav, A.I. Yavin, S. Yen, Phys. Rev. D **49**, 3120 (1994).
26. K. Konno, H. Nakamura, Lett. Nuovo Cimento **34**, 313 (1982); K. Konno, H. Nakamura, H. Noya, Phys. Rev. D **35**, 239 (1987); N. Konno, Nuovo Cimento A **111**, 1393 (1998); H. Noya, H. Nakamura, *Proceedings of the IX International Conference on Hadron Spectroscopy, Protvino, Russia, 2001*, AIP Conf. Proc., edited by D. Amelin (AIP, 2002) p. 533.
27. T.T. Nakamura, H. Kobayashi, A. Konaka, K. Imai, A. Masaike, K. Miyake, T. Nagamine, N. Sasao, Y. Yamada, Phys. Rev. C **39**, 1261 (1989).
28. H. Garcilazo, A. Valcrace, F. Fernandez, Phys. Rev. C **64**, 058201, (2001).
29. P.J. Mulders, A.T. Aerts, J.J. de Swart, Phys. Rev. D **19**, 2635 (1979).
30. A.P. Kobushkin, nucl-th/9804069.
31. T. Walcher, hep-ph/0111279.
32. Y.E. Pokrovsky, *Proceedings of the 7th International Conference on Hadron Spectroscopy "Hadron'97"*, edited by S.U. Chung, H.J. Wilutzky (AIP, Upton, NY, 1997) p. 409; *Proceedings of the XXXIII International Winter Meeting on Nuclear Physics, Bormio (Italy), 1995*, edited by I. Iori, Suppl. N. **101**, 540 (1995).
33. C. Helminen, D.O. Riska, *Proceedings of the Workshop on the Physics of Excited Nucleons, NSTAR 2001, Mainz*, edited by D. Drechsel, L. Tiator (World Scientific, Singapore, 2001) p. 217.
34. L.V. Fil'kov, nucl-th/0208028.
35. S. Simula, *Proceedings of the Workshop on The Physics of Excited Nucleons, NSTAR 2001, Mainz*, edited by D. Drechsel, L. Tiator, (World Scientific, Singapore, 2001) p. 135.
36. L. Theussl, R.F. Wagenbrunn, B. Desplanques, W. Plessas, Eur. Phys. J. A **12**, 91 (2001).